NASA/TM–20230012868

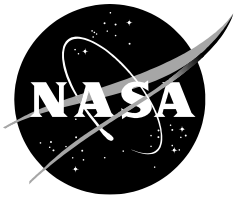

Performance of Two Battery Prognostic Applications used by Two Octocopters for Safe Low Altitude Autonomous Flight Operations

Edward F. Hogge
ViGYAN, 30 Research Drive, Hampton, Virginia

Chetan S. Kulkarni
KBR Wyle Services, Inc., Ames Research Center, Moffett Field, California

Kenneth W. Eure, Kaveh Darafsheh, *Sixto L. Vazquez, Kyle M. Smalling, Cuong C. Quach*
Langley Research Center, Hampton, Virginia

June 2024

NASA STI Program Report Series

Since its founding, NASA has been dedicated to the advancement of aeronautics and space science. The NASA scientific and technical information (STI) program plays a key part in helping NASA maintain this important role.

The NASA STI program operates under the auspices of the Agency Chief Information Officer. It collects, organizes, provides for archiving, and disseminates NASA's STI. The NASA STI program provides access to the NTRS Registered and its public interface, the NASA Technical Reports Server, thus providing one of the largest collections of aeronautical and space science STI in the world. Results are published in both non-NASA channels and by NASA in the NASA STI Report Series, which includes the following report types:

- TECHNICAL PUBLICATION. Reports of completed research or a major significant phase of research that present the results of NASA Programs and include extensive data or theoretical analysis. Includes compilations of significant scientific and technical data and information deemed to be of continuing reference value. NASA counterpart of peer-reviewed formal professional papers but has less stringent limitations on manuscript length and extent of graphic presentations.

- TECHNICAL MEMORANDUM. Scientific and technical findings that are preliminary or of specialized interest, e.g., quick release reports, working papers, and bibliographies that contain minimal annotation. Does not contain extensive analysis.

- CONTRACTOR REPORT. Scientific and technical findings by NASA-sponsored contractors and grantees.

- CONFERENCE PUBLICATION. Collected papers from scientific and technical conferences, symposia, seminars, or other meetings sponsored or co-sponsored by NASA.

- SPECIAL PUBLICATION. Scientific, technical, or historical information from NASA programs, projects, and missions, often concerned with subjects having substantial public interest.

- TECHNICAL TRANSLATION. English-language translations of foreign scientific and technical material pertinent to NASA's mission.

Specialized services also include organizing and publishing research results, distributing specialized research announcements and feeds, providing information desk and personal search support, and enabling data exchange services.

For more information about the NASA STI program, see the following:

- Access the NASA STI program home page at http://www.sti.nasa.gov

- Help desk contact information:

https://www.sti.nasa.gov/sti-contact-form/
and select the "General" help request type.

NASA/TM–20230012868

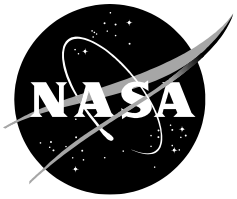

Performance of Two Battery Prognostic Applications used by Two Octocopters for Safe Low Altitude Autonomous Flight Operations

Edward F. Hogge
ViGYAN, 30 Research Drive, Hampton, Virginia

Chetan S. Kulkarni
KBR Wyle Services, Inc., Ames Research Center, Moffett Field, California

Kenneth W. Eure, Kaveh Darafsheh, Sixto L. Vazquez, Kyle M. Smalling, Cuong C. Quach
Langley Research Center, Hampton, Virginia

National Aeronautics and
Space Administration

Langley Research Center
Hampton, Virginia

June 2024

Acknowledgments

The authors would like to thank NASA's Aeronautics Research Mission Directorate for its support through the System-Wide Safety project. Thanks to pilot Nicholas H. Rymer for research multirotor flights. We also would like to recognize intern Eric J. Miers for the Python code that enabled plotting of the battery model results and to recognize intern Carissa Hardy for the propulsion efficiency analysis.

Available from:

NASA STI Program / Mail Stop 148
NASA Langley Research Center
Hampton, VA 23681-2199

Abstract

This paper addresses the problem of building trust in online predictions of the remaining available flying time for two different electric Unmanned Aerial Vehicles (eUAVs) powered by lithium-ion-polymer batteries. Flight tests for various automation research missions for the two vehicles were monitored using two on-board battery health management applications. These applications made predictions of the remaining flying time (RFT) for each eUAV and predicted the charge state of the battery. Playback of the voltage, current and temperature profiles of the battery discharge were used to assess the accuracy of the estimation of the voltage and the charge states of the models as well as their estimate of the RFT. The reference ground truth values were the observed landing time and the measured battery pack resting voltage 20 minutes after the flight. The predicted RFT, state of charge (SoC), and state of energy (SoE) were compared with the observed results. Noise values of one standard deviation from the mean values of the internal charge states of the battery model during a reference run were used to vary the states during simulation. One application used an equivalent circuit model of the electrical dynamics of the battery pack, and the other application used a reduced-order electrochemistry model. The variation of the model state components was compared to the variation in the estimate of the RFT and the variation in the SoE to estimate a confidence factor. Variation in the estimates caused by factors affecting the off-line laboratory parameter identification experiments is considered. Variation in the estimates due to environmental factors is discussed.

1. Introduction

The remaining flying time (RFT) of battery-powered multirotor electric Unmanned Aerial Vehicles (eUAVs) is of interest to the user community, civilian and military, who would like to use them to perform various tasks at a lower cost relative to that of a general aviation alternative. The cost effectiveness and safety of eUAV use depends upon a reliable estimate of the RFT. The safety of the low altitude eUAV's autonomous interaction with other users of the airspace depends upon a reliable estimate of RFT for the planned flight path and any contingency flight path.

There is a long history of experience with petroleum-based fuels for commercial aviation. The remaining flying time for this fuel is based upon the easily measured quantity in the fuel tank. There are several ways in which predicting remaining operating time is more complicated for battery-powered vehicles than for vehicles with a conventionally powered liquid-fueled combustion system. Unlike a liquid-fueled system, where the fuel tank's volume remains unchanged over successive refueling operations, a battery's charge storage capacity will diminish over time. Another complicating feature of a battery system is the time-varying relationship between battery output power and battery current draw. Whereas a conventional liquid combustion system uses an approximately constant amount of liquid fuel to produce a given motive power, the power from a battery system is equal to the product of battery voltage and current. Thus, as batteries are discharged, their voltages drop lower, and they lose charge at a faster rate to maintain a specific power output.

For a multirotor eUAV the stored battery energy is accessed through varying the resistance of a transistor circuit in an electronic speed controller following a commanded input signal. As the resistance of the transistors in the electronic speed controller reduces, the current demand from the battery increases. This produces a consequent drop in the battery voltage. Hence the control signal causes a change in current which results in a change in voltage.

There is a relationship between the charge stored in the battery and the voltage presented at the terminals during the equilibrium condition (Atkins, de Paula &

Keeler, 2018). However, during operation there are time lags between the amount of charge presented at the terminals that comes from the surface of the electrode and the amount of the charge stored in the bulk electrolyte between the electrodes and the half-cell separator. The charge at the terminals produces an electrical potential (voltage) which can be measured easily. These time lags are called the battery electrodynamics and they make it difficult to estimate the charge remaining in the battery during use.

As an example, consider a constant-current discharge of a battery. The trend in the voltage follows that of the plot in Fig. 1 (after Saxena, Celaya, Roychoudhury, Saha, Saha, and Goebel, 2012). We modified the figure to use the laboratory discharge data from our battery D027 that discharged at a rate that would fully discharge the battery in one hour to illustrate. This plot consists of three different regions. The first two regions are approximately linear followed by a third region with a sharp non-linear voltage drop-off. The first near-linear region is the initial drop in voltage upon application of the load current demand to hover the vehicle at takeoff. The second near-linear region (most of the plot) covers the discharge profile where the voltage drops proportionately to the discharge of the charge contained in the battery. The slope of this section is affected by the load current, which for the multirotor case is mostly constant. This region ends with the start of the voltage drop-off region. This steep drop-off section is nonlinear and comes with an increase in the slope of the discharge at the beginning of the nonlinear region. The location of this slope steepening is called the “knee point”. (Saxena et al. 2012) reports that the battery has depleted approximately 90 percent of its available charge before encountering this “knee point”. The six-cell lithium-ion-polymer batteries used for our multirotor vehicles are considered fully discharged (100 percent depth of discharge) when they have reached 18.0V in a controlled low current discharge laboratory experiment.

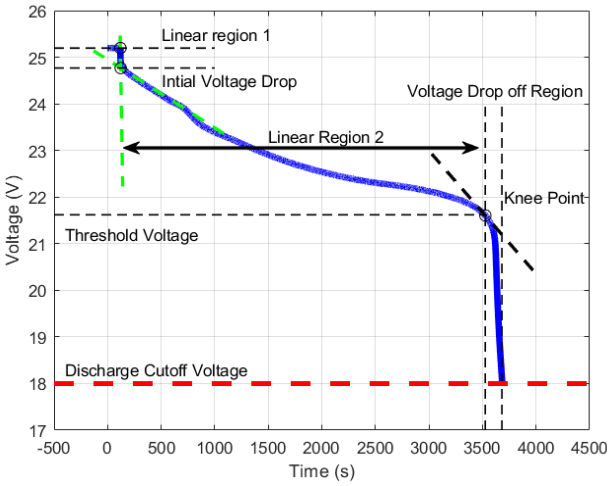

Figure 1. Battery discharge terminology.

We flew two octocopter multirotor vehicles for the study. The first one flown was a modified DJShenzhen DJI Sciences and Technologies Ltd. S1000 octocopter without the DJI navigation components that we named “Cerf” (Fig. 2). This vehicle was used in the 2018 to 2019 time frame before NASA was prohibited to use DJI equipment. Cerf weighed 20 to 25 pounds (9.1 to 11.3 kg) depending upon the research payload. The airframe is constructed of carbon fiber. The powertrain consists of eight S800 EVO Electronic Speed Controllers (ESC) each driving one of eight 4114 PRO brushless motors. Each motor drives a 1552 folding propeller. The propellers alternate direction of rotation clockwise and counterclockwise in an “octo X” configuration.

Figure 2. DJI S1000 eUAV Cerf.

Figure 3. Tarot T18 eUAV Aragog.

The second vehicle flown was a Tarot 18 octocopter we named “Aragog” (Fig. 3). Aragog weighed 25 to 29 pounds (11.3 to 13.2 kg) with a more complex research payload than Cerf. It is constructed of carbon fiber as well. The powertrain has eight KDE-UAS40UVC ESCs each driving one of eight KDE4213XF-360 brushless motors. Each motor drives a Tarot High Efficiency 1855 propeller. The propellers also alternate direction of rotation as seen with the vehicle Cerf.

Onboard battery discharge prognostic algorithms estimate the state of charge (SoC) expressed as a fraction of 1.0 for fully charged to 0.0 for fully discharged and predict the RFT for motor batteries using the steps outlined below and in Fig 4.

1 Estimate the current battery state.

2 Use the unscented Kalman filter (UKF) Bayesian estimator to update the battery state based on voltage and current measurements at the battery pack output terminals.

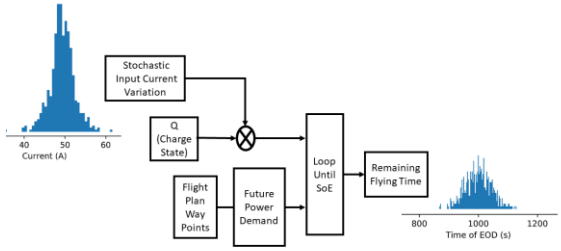

Figure 4. Input current variation added to charge states to estimate RFT.

3 Forecast the future state using the battery model and expected power demand based upon flight plan distance and ground speed to estimate the flight time with a hovering load.

4 RFT prediction uses the UKF estimator to simulate the future battery state until a simulated discharge crosses a threshold of 20 percent SoC. This can be scaled by the model estimated voltage to estimate the battery’s SoE (Fig 12).

The 20 percent SoC threshold will keep the models from instabilities encountered below 5 percent SoC. The heating from the increased current and the internal resistance prematurely ages the battery at low SoC as well. We have used and will describe the performance of two battery health models to estimate SoC and RFT. The first model considered is a simple equivalent circuit model following (Daigle and Sankararaman, 2016) and (Jiang, Wang, Wu, Etse-Dabu & Xiong, 2020). We will refer to it as “Circ”. The second model uses a basic chemistry and physics-based model, (Daigle & Kulkarni, 2013). It is an electrochemistry battery health model which we will refer to as “Chem”. Both models are implemented using a Bayesian belief subjective approach through an optimal unscented Kalman filter.

Kalman filtering is an established technology used since the Apollo program, (Grewal & Andrews, 2010) for the estimation of states within a dynamic system. For linear systems, this method of state estimation is optimal. The Kalman filter consists of a set of recursive equations that are evaluated repeatedly and updated using input/output measurements as the system operates (section 4.3, page 56 of Särkkä, 2013). The mathematical model of the system consists of two noise sources: process noise and measurement noise. Process noise is noise in the state estimate due to systemic modeling errors, inaccuracies and model parameter identification errors. Measurement noise

consists of sensor errors and electrical noise. For linear observable systems with known process and measurement noise variances, the Kalman filter has been widely employed as the optimal state estimator. However, many systems are nonlinear. In our case, the battery discharge voltage profile is a nonlinear function of the input power demand (current demand).

Each model's battery capacity, internal resistance and other parameters were identified through three laboratory experiments that used a programmable load, (Eure & Hogge, 2020). In the first experiment, batteries were slowly discharged at 1/50-C constant current to an open circuit voltage of 16V. (here, one-C is the current necessary to completely discharge the battery in one hour, not one coulomb). In the second experiment the battery was discharged with a constant load of one-C to discharge the battery to the minimum safe charge state in approximately one hour. Hence the first experiment takes 50 hours for a battery to reach the cut-off SoC threshold. The second one- C discharge experiment was used to identify the dynamical parameters of the battery model. The third discharge experiment used variable loads similar to those expected during operation of the vehicle to fit any remaining parameters and to scale the discharge model to the vehicle size. The software algorithms were derived from the GitHub Prognostics Model Library (Daigle, 2016b) and the Prognostics Algorithm Library, (Daigle, 2016a) written in MATLAB. We used the Generic System for Prognostics (GSAP) open-source library of some of the MATLAB modules translated into C++. We adapted some of the modules released to GitHub in 2018 (Teubert, Daigle, Sankararaman, Watkins, and Goebel, 2016). Our code used a general-purpose satellite operating system, the Core Flight System (CFS). NASA Goddard Space Flight Center developed CFS to build control systems for satellites, from small CubeSats to Hubble class satellites that perform diverse missions and use a common set of libraries and re-use philosophy, (NASA, Goddard Space Flight Center, 2019). We extended the use of CFS to the multirotor drones as part of the System-Wide Safety project, (Young, Ancel, Moore, Dill, Quach, Foster, Darafsheh, Smalling, Vazquez, Evans, Okolo, Corbetta, Ossenfort, Watkins, Kulkarni, and Spirkovska, 2020). Class diagrams of the GSAP modules employed in our RFT estimation software are shown in Appendix B.

This paper is organized as follows:

- Table of Symbols, Table 1
- Table of Abbreviations, Table 2
- Section 2 is the theoretical framework for the battery prognostic modeling and unscented Kalman filter observer.
- Section 3 has the momentum theory used for the propeller load demand calculations, and the framework for estimating uncertainty in the RFT prediction.
- Section 4 describes the equivalent circuit battery prognostic model Circ.
- Section 5 describes the electrochemistry battery prognostic model Chem.
- Section 6 describes the process used to tune and compare the models.
- Section 7 reviews the identification of the model parameters from laboratory discharge experiments.
- Section 8 reports on the lessons learned.
- Section 9 presents the results of the flight tests of the two flight campaigns with each vehicle.
- Section 10 summarizes conclusions.

Table 1. Symbols

α	Lithium-intercalated host material of an ideal battery (Chem) (subscript)
α_V	Angle of tilt of the rotor disk or thrust platform (degrees)
β	Unoccupied host material of an ideal battery (Chem) (subscript)
$\gamma_{\alpha,n}$	Activity coefficient that accounts for the deviation the activity of a real solute from ideal Henry's law behavior for the lithium-intercalated host material, negative electrode case. (Chem) (fraction)
$\gamma_{\alpha,p}$	Activity coefficient that accounts for the deviation the activity of a real solute from ideal Henry's law behavior for the lithium-intercalated host material, positive electrode case. (Chem) (fraction)
ρ	Air density (kg/m^3)
$\boldsymbol{\theta}(k)$	Model parameter vector at time step k ,for our case the parameters are identified off-line and assumed to be constant, θ_c, for a given flight
μ	Mean from statistics
$\boldsymbol{\Xi}$	Uncertain concatenated vector of model inputs $[\boldsymbol{x}(\boldsymbol{k_p}), \boldsymbol{U_{k_p}}, \boldsymbol{\Theta_{k_p}}, \boldsymbol{V_{k_p}}]$
ξ	Realization of the uncertain concatenated vector of model inputs $\boldsymbol{\Xi}$
σ	Standard deviation from statistics
$\phi_s(0,t)$	Potential at the positive current collector (Chem) (V)
$\phi_s(L,t)$	Potential at the negative current collector (Chem) (V)
a_α	Activity of solvent for lithium-intercalated host material. (chem) (fraction)
a_β	Activity of solvent for unoccupied host material. (chem) (fraction)
A	Rotor disc actuactor area (m^2)
$A_{n,j}$	Fitting parameter for Redlich-Kister expansion for the negative electrode excess Gibbs free energy activity coefficient (Chem)
$A_{p,j}$	Fitting parameter for Redlich-Kister expansion for the positive electrode excess Gibbs free energy activity coefficient (Chem)
$c_{b,n}$	Concentration of the negative bulk electrolyte charge (Chem) (coulombs m^{-3})
$c_{b,p}$	Concentration of the positive bulk electrolyte charge (Chem) (coulombs m^{-3})
$c_{s,n}$	Concentration of the negative electrode surface charge (Chem) (coulombs m^{-3})
$c_{s,p}$	Concentration of the positive electrode surface charge (Chem) (coulombs m^{-3})
C_b	The large capacitor capacitance that is a empirical nonlinear power series function of SoC (Daigle et al. 2016) (Circ) (F)

Table 1. Symbols Continued

Cb_0	The large capacitor capacitance when the battery is charged before the flight. (Daigle et al. 2016) (Circ) (F)
$Cbp_0, Cbp_1, Cbp_2, Cbp_3$	Fitted parameters for power series fit to laboratory discharge experiment data. (Daigle et al. 2016) (Circ)
C_{max}	The maximum charge that can be drawn from a battery in practice (Circ, Chem) (coulombs)
C_s	Capacitance of the resistor and capacitor pair that captures the ohmic voltage drop of the (Daigle et al. 2016) (Circ) (F)
C_p	Capacitance of the parallel resistor and capacitor pair (Jiang et al. 2020) (Circ) (F)
C_{sp}	Capacitance of the resistor and capacitor pair that captures the nonlinear voltage drop due to the surface overpotential (Daigle et al. 2016) (Circ) (F)
E	Event state change
F	Faraday's constant (coulombs/mole of charge carriers)
$\mathbf{f}()$	State equation function operator, outputs a state vector
$\mathbf{h}()$	State space output function operator, outputs a state vector
i, i_b, I(t)	Discharge current for the equivalent circuit model (Circ) (A)
i_{app}	Applied electric current input vector component (Chem) (A)
i_P	Current through the parasitic load resistor. (not shown, Fig. 10) (Circ) (A)
i_s	Current through capacitor C_s., Fig. 10 (Circ) (A)
i_{sp}	Current through capacitor C_{sp}., Fig. 10 (Circ) (A)
J_n	Current density of the negative electrode (Chem) (Am^{-2})
J_p	Current density of the positive electrode (Chem) (Am^{-2})
J_{n0}	Exchange current density of the negative electrode (Chem) (Am^{-2})
J_{p0}	Exchange current density of the positive electrode (Chem) (Am^{-2})
k	Discrete time step of the state space model
$\triangle k$	The difference between the time of the threshold event and the time of the start of prediction
k_E	Time that event E occurs
$\triangle k_{\mathrm{E}}(k_{\mathrm{P}})$	The time remaining until event E occurs
k_P	Time when a prediction is performed
n	The number of electrons transferred in the cell reaction (model Chem)
$\mathbf{n}(k)$	Vector of Gaussian sensor noise at time step k
P	Total power demand on the battery (W)
P_h	Power to hover a vehicle per rotor (W)
q_b	Charge on large capacitor C_b. First component of the state vector (Circ) (coulombs)
$\dot{q_b}$	Time rate of change of charge on large capacitor C_b. (Circ) (coulombs/s)

Table 1. Symbols Continued

$q_{b,n}$	State vector component of the negative bulk electrolyte charge (Chem) (coulombs)
$q_{b,p}$	State vector component of the positive bulk electrolyte charge (Chem) (coulombs)
$\dot{q}_{b,n}$	The negative bulk electrolyte charge rate of change (Chem) (A)
$\dot{q}_{b,p}$	The positive bulk electrolyte charge rate of change (Chem) (A)
$\dot{q}_{bs,n}$	The negative electrode charge diffusion rate from the bulk electrolyte to the surface (Chem) (A)
$\dot{q}_{bs,p}$	The positive electrode charge diffusion rate from the bulk electrolyte to the surface (Chem) (A)
q_{max}	The maximum charge that the battery can hold (Circ, Chem) (coulombs)
q_n	Charge of the negative electrode surface and bulk electrolyte (Chem) (coulombs).
q_p	Charge of the positive electrode surface and bulk electrolyte (Chem) (coulombs).
$q_{s,n},\ q_{s,n}(k)$	State vector component of the negative electrode surface charge (Chem) (coulombs)
$\dot{q}_{s,n}$	The negative electrode surface charge rate of change (Chem) (A)
$q_{s,p},\ q_{s,p}(k)$	State vector component of the electrochemistry model for the positive electrode surface charge (coulombs)
$\dot{q}_{s,p}$	The positive electrode surface charge rate of change (Chem) (A)
q_{sMax}	The maximum charge that the battery electrode surface can hold (Chem) (coulombs)
$q_{s,n,max}$	The maximum charge that the negative battery electrode surface can hold (Chem) (coulombs)
$q_{s,p,max}$	The maximum charge that the positive battery electrode surface can hold (Chem) (coulombs)
q_{sp}	Charge on equivalent circuit model "Circ" small capacitor C_{sp}. Second component of the state vector. (coulombs)
$\dot{q_{sp}}$	Time rate of change of charge on small capacitor C_{sp}. of the equivalent circuit model "Circ". (coulombs/s)
$\mathbf{Q}$	Process noise covariance matrix
R	The set of predictions that is uncertain
R	The universal gas constant (Chem). $(JK^{-1}mol^{-1})$
R_0	Resistance that captures the ohmic voltage drop (Jiang et al. 2020) (ohms)
R_p	Resistance of the parallel resistor and capacitor pair (Jiang et al. 2020) (ohms)
R_s	Resistance of the resistor and capacitor pair that captures the ohmic voltage drop (Daigle et al. 2016) (ohms)

Table 1. Symbols Continued

R_{sp}	Resistance of the resistor and capacitor pair that captures the nonlinear voltage drop due to the surface overpotential which is a function of SoC (Daigle et al. 2016) (Circ) (ohms)
$R_{sp0}, R_{sp1}, R_{sp2}$	Fitted parameters for exponential fit to laboratory discharge experiment data as a function of SoC. (Daigle et al. 2016) (Circ)
R_{th}	Series resistance of the Thévenin equivalent circuit model (ohms)
$\boldsymbol{r}$	A realization of R, the set of predictions that is uncertain
$\mathbf{R}$	Measurement noise covariance
SoC	State of Charge of the battery (fraction)
SoE	State of Energy of the battery (fraction)
t	Continuous time (s)
$t_{Diffusion}$	Diffusion time constant of the diffusion rate of the Li ions moving from the bulk electrolyte to the surface of the electrode
T	Total thrust of the rotor actuator disks of the vehicle (newton)
T	The electrode temperature (model Chem) (kelvins)
T_E	Earliest time that some boolean event changest from false to true
T_V	Vertical vehicle thrust component (newton)
Δt	Discrete time step *k* sampling period. (s)
$\mathbf{u}(k)$	State space model input vector at time step k
U	Total voltage across the resistor and resistor-capacitor pair (Jiang et al. 2020)
$U_{o,n}$	Reference potential of an ideal battery at the negative battery terminal. (V)
$U_{o,p}$	Reference potential of an ideal battery at the positive battery terminal. (Chem) (V)
U_L	Battery terminal voltage (Jiang et al. 2020)
$U_{oc}(SoC)$	Battery open-circuit voltage as function of State of Charge (Jiang et al. 2020)
$\mathbf{v}(k)$	Vector of Gaussian model process noise at time step k
V_0	Initial voltage of the battery at rest before take-off (V)
V_η	Overpotential voltage, difference in cell voltage and that applied to the cell under working conditions (Butler-Volmer equation A.24)
$V'_{\eta,n}$	State vector component of the electrochemistry model for the voltage due to overpotential, negative electrode.(V)
$V'_{\eta,p}$	State vector component of the electrochemistry model for the voltage due to overpotential, positive electrode.(V)
V'_o	State vector component of the electrochemistry model for the voltage due to the sum of the ohmic voltage contributions overpotential (V)

Table 1. Symbols Continued

$V_{INT,n}$	Activity correction term of the nonideal battery, negative electrode (Chem)
$V_{INT,p}$	Activity correction term of the nonideal battery, positive electrode (Chem)
V_m	Estimated modeled output voltage, component of output vector (Circ, Chem) (V)
V	Total voltage of the battery stack. This multiplied with power demand gives the total power demand (V)
V_p	Voltage across the parallel resistor and capacitor pair (Jiang et al. 2020) (Circ) (V)
V_s	Voltage across resistor R_s., Fig. 10 (Circ) (V)
V_{sp}	Voltage across capacitor C_{sp}., Fig. 10 (Circ) (V)
V_{th}	Ideal voltage source of the Thévenin equivalent circuit model (V)
$V_{U,n}$	Voltage at negative terminal of an ideal battery (Chem) (V)
$V_{U,p}$	Voltage at positive terminal of an ideal battery (Chem) (V)
W	Vehicle weight (N)
x_n	Mole fraction of the negative electrode surface and bulk electrolyte charge (Chem) (fraction).
x_p	Mole fraction of the positive electrode surface and bulk electrolyte charge (Chem) (fraction).
$x_{b,n}$	Mole fraction of the charge carriers in the bulk electrolyte near the negative electrode (Chem) (fraction)
$x_{b,p}$	Mole fraction of the charge carriers in the bulk electrolyte near the positive electrode (Chem) (fraction)
$x_{s,n}$	Mole fraction of the charge carriers on the surface of the negative electrode (Chem) (fraction)
$x_{s,p}$	Mole fraction of the charge carriers on the surface of the positive electrode (Chem) (fraction)
$\mathbf{x}(k)$	Vector of state space model states (state vector) at time step k
$\mathbf{y}(k)$	State space model output vector at time step k

Table 2. Abbreviations

1/50-C	1/50 of the current necessary to completely discharge a battery in one hour, not 1/50 coulomb
One-C	The current necessary to completely discharge a battery in one hour, not one coulomb
6S2P	Battery with two parallel sets of 6 cells in series
Aragog	Modified Tarot 18 octocopter named after a spider Harry Potter character
Cerf	Modified DJShenzhen DJI Sciences and Technologies Ltd. S1000 octocoptor named after Dr. Vinton Cerf, American Internet pioneer
CFS	Core Flight System general-purpose satellite operating system
Chem	Battery state space model using reduced-order chemistry and physics equations
Circ	Battery state space model using an equivalent circuit electrical analogy
ESC	Electronic Speed Controller
eUAV	Electric Unmanned Aerial Vehicle
GitHub	Open-source software Internet site
GSAP	Generic System for Prognostics, C++ open-source software library
IQR	Interquartile range from rank order statistics
LiPo	Lithium-ion Polymer battery
Octo X	Multirotor propeller rotation configuration with eight rotors, numbered clockwise one to eight, rotor one opposite rotor eight. Rotor one rotates clockwise, rotor two counter clockwise, in an alternating pattern for all rotors.
RFT	Remaining Flying Time
SoC, SOC	State of Charge
SoE	State of Energy
UKF	Unscented Kalman Filter Bayesian estimator

2. Model-Based Approach and Previous Work

There have been various strategies used to estimate battery SoC. Some have employed table lookups from laboratory discharge experiments while others have proposed data-driven approaches that use the discharge histories and neural networks (Saxena et al. 2012). Our approach follows the use of physical laws to create the estimates of the model parameters. We use laboratory experiments to estimate the model parameters under controlled conditions. These model parameters are further tuned through use of ground truth values observed from the laboratory experiments and adjusted by field experiments with the multirotor vehicles. The primary truth value used is the actual flying time supplemented by the secondary truth value of charge remaining in the battery at landing (SoC). SoC is looked up from the low-current discharge graph using the input of resting voltage measured one hour after landing by a calibrated voltmeter.

2.1 Generic system representation for prediction for both Circ and Chem models

We use a model-based generic system representation as in (Daigle & Goebel, 2013). This consists of a system being monitored and a developed model that describes system changes in response to its inputs. The generic system is represented by a state space model:

$$\mathbf{x}(k+1) = \mathbf{f}(k, \mathbf{x}(k), \boldsymbol{\theta}(k), \mathbf{u}(k), \mathbf{v}(k)) \quad (1)$$

$$\mathbf{y}(k) = \mathbf{h}(k, \mathbf{x}(k), \boldsymbol{\theta}(k), \mathbf{u}(k), \mathbf{n}(k)) \quad (2)$$

k is the discrete time variable. In our case *k* increments by one second each step. The state definition, the input, the output, and the relevant model variables are defined in Eq. set 3a for model Circ.

$$\mathbf{x}(k) = [\, q_b \;\; q_{sp} \,]$$
$$\mathbf{u}(k) = [\, P \,]$$
$$\mathbf{y}(k) = [\, V \,] \quad (3a)$$

The model Circ state vector $\mathbf{x}(k)$ consists of the charge q_b, on the large capacitor C_b, the charge q_{sp} on the small capacitor C_{sp} (see Fig. 10). The input vector is the power demand P. The output vector consists of the battery model voltage V, V_m.

The state definition, the input, the output, and the relevant model variables are defined in Eq. set 3b for model Chem.

$$\mathbf{x}(k) = [\, q_{s,p} \; q_{b,p} \; q_{b,n} \; q_{s,n} \; V_o' \; V_{\eta,p}' \; V_{\eta,n}' \,]$$
$$\mathbf{u}(k) = [\, i_{app} \,]$$
$$\mathbf{y}(k) = [\, V \,] \quad (3b)$$

The model Chem state vector $\mathbf{x}(k)$ consists of the positive electrode surface charge $q_{s,p}$, the positive electrode bulk charge $q_{b,p}$, the negative electrode bulk charge $q_{b,n}$, the negative electrode surface charge $q_{s,n}$, the sum of the ohmic voltage contributions V_o', the positive electrode overpotential $V_{\eta,p}'$, and the negative electrode overpotential $V_{\eta,n}'$ (see Appendix A for details). The input vector consists of the discharge current i_{app}. The output vector consists of the battery model voltage V, V_m.

$\boldsymbol{\theta}(k)$ is the model parameter vector; $\mathbf{v}(k)$ is the process noise vector; $\mathbf{f}$ is the state equation; $\mathbf{y}(k)$ is the output vector; $\mathbf{n}(k)$ is the sensor noise vector; and $\mathbf{h}$ is the output equation. We are interested in predicting the occurrence of an event E as the earliest instant that some Boolean event threshold T_E changes from zero (false) to one (true). Let k_E denote the time at which the event E occurs and let k_P denote the time when we perform a prediction.

$$k_{\mathrm{E}}(k_{\mathrm{P}}) \triangleq \inf\{k \geq k_{\mathrm{P}} \wedge T_{\mathrm{E}}(\mathbf{x}(k), \boldsymbol{\theta}(k), \mathbf{u}(k)) = true\} \quad (4)$$

To explain the notation:

$x \triangleq y$ means that x is defined to be equal to y .

inf() is the infimum operator which is the greatest lower bound of a nonempty subset of a partially ordered set of real numbers.

$x \wedge y$ means the logic operation on $x \; and \; y$.

$k_{\mathrm{E}}(k_{\mathrm{P}})$ is the time of the event at the prediction simulation time step k_P. This occurs at the greatest lower bound of the steps when the event threshold T_E is $true$. We point out that k_E is a function of the time of prediction k_P, since the time of event E depends upon the model's state at k_P and future conditions. We can define the time remaining until the event E occurs as:

$$\triangle k_{\mathrm{E}}(k_{\mathrm{P}}) \triangleq k_{\mathrm{E}}(k_{\mathrm{P}}) - k_{\mathrm{P}} \quad (5)$$

This is the symbolic definition of the remaining flying time in discrete time k.

2.3 Simplifying assumptions for our multirotor use case

1) $\mathbf{u}(k)$ is the input (or control) vector and its mean value is a constant once flying since greater than 90 percent of the thrust is expended to hover the vehicle (see below) and is primarily a function of weight and the

distribution is approximately Gaussian (normal distribution). Additionally, we assume the future inputs are known and are nearly constant.

2) $\boldsymbol{\theta}(k)$ is the model parameter vector. The parameters are identified off-line and are assumed to be constant during the duration of any given flight. $\boldsymbol{\theta}(k) = \theta_c$

3) $\mathbf{v}(k)$ is the model process noise for the Kalman filter. It is assumed to be a stationary, Gaussian, white noise sequence. (See prediction uncertainty section below). (Daigle et al. 2016) made similar assumptions as they stated: "In our system all parameters are assumed to be known… The effect of process noise is negligible relative to the uncertainty in future inputs".

We estimate the state of the battery by Bayesian filtering. Bayesian filtering refers to a method of estimating the internal state of a time-varying system which is indirectly observed using noisy measurements (measurement noise covariance $\mathbf{R}$). Since the measurements have noise, they are uncertain. In our case the state of the system is described by the charge contained in the battery. This charge is represented by either the charge of an analogous capacitor from an equivalent electrical circuit (model Circ), or the mole fraction of the ions in the bulk electrolyte or the mole fraction of the charge carriers at the surface of the cathode and the anode electrodes (model Chem). The state of the system changes in time can be modeled as a dynamic system perturbed by a process noise covariance $\mathbf{Q}$ (Sarkka, 2013).

2.4 Unscented Kalman filter as State Observer for both Circ and Chem Models

The unscented Kalman filter (UKF) is used to provide an estimate of the charge state based upon the measured battery voltage and current (power) demand made on the battery. The UKF is based on the *unscented transform* (Julier & Uhlmann, 1997) that choses a fixed number of special points "sigma points" to capture the mean and covariance of the original distribution of state values. The use of sigma implies the standard deviation of the distribution. Just these sigma points are propagated through the non-linear model to represent the propagation of the associated distribution. The mean and covariance of the transformed state values are estimated from these transformed points. This is described in detail on (page 81-86 of Sarkka, 2013) and in section "Estimation" of (Daigle et al. 2016).

The UKF is a tool for computing probabilistic belief in system state estimates based on stochastic models of the system's dynamics. The UKF assumes a general non-linear form of the state and output equations, and efficiently propagates model and state uncertainties as indicated in the "observer" block of Fig. 5. The UKF employs an unscented transform using a minimal set of weighted samples, called sigma points, whose mean, and covariance are preserved once transformed by the unscented transform and by the nonlinear battery model function (Julier & Uhlmann, 1997, 2004). The UKF takes battery power demand (function of current demand) as a controlling input to the system, and the measured battery voltage from the previous time step. The UKF gives a probability distribution for charge state variables and the future voltage state output distribution. The SoC distribution can be directly derived from this. To perform the prediction function indicated in the "prediction" block of Fig. 5, the future system state is simulated until a given cut-off threshold is reached for each sampled sigma point, (Daigle et al. 2012). Readers interested in the application of the

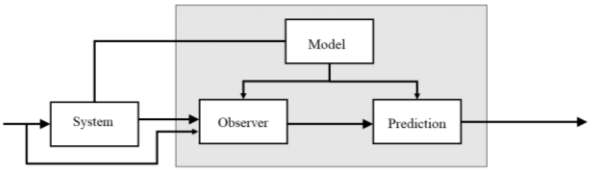

Figure 5. Model-based RFT prediction (after Sierra, Orchard, Goebel, and Kulkarni, 2018).

UKF to the estimation of battery SoC are referred to our previous papers (Bole et al. 2013); (Daigle et al. 2012) and the references therein. The Bayesian use of actual past system behavior makes the model-based filtering approaches such as UKF much less susceptible to initialization and measurement errors than the coulomb counting method currently used in many battery monitoring systems (Dai et al. 2006).

3. Battery Capacity Modeling for Remaining Flying Time

Batteries are complex electrochemical systems. The chemical reactions have been studied since the eighteenth and nineteenth century by Michael Faraday, Luigi Galvani, Alessandro Volta and others, including (Galvani, 1791), (Volta, 1800), (Faraday, 1834). At the core, the chemical reactions are quantum phenomena and complex. We use the high-level battery pack view of a battery with simplified equations to model it. It does not differ greatly from the electrochemical cell of the 1800s studied by M. Faraday and W. Nernst. Our use case consists of solid-state motor control circuits and propellers with loading due to the local flow field that can be complex. We make simplifying assumptions and use the simple Momentum Theory and Actuator Disk Theory of (Stepniewski, 1979) to get a 95 percent accurate estimate of actuator disk loading and associated electrical power demand (current demand) on the battery. The actuator disk equations are computationally efficient, and the accuracy is no worse than the accuracy of the battery models we use.

3.1. Future power demand

In our previous work we used battery-powered fixed-wing vehicles, (Hogge, Bole, Vazquez, Celaya, Strom, Hill, Smalling, & Quach, 2015), (Quach, Bole, Hogge, Vazquez, Daigle, Celaya, Weber, & Goebel, 2013). Multirotor vehicles that hover have a different energy consumption model. In both vehicles, the future power demand has a major influence on the remaining flying time (RFT).

3.2. Calculation of thrust power to electrical power efficiency

One way to think about multirotor vehicle power demand is to take the static forces of the hovering case to approximate our power demand by assuming the vehicle weight W equals the vertical component T_V of the total thrust T. Since the vehicle is not ascending or descending from an imbalance in the vertical forces, the vertical thrust component is the projection of the thrust on the vertical axis and is given by Eq. (6) from page 66 of Stepniewski, (1979). See the free-body diagram in Fig. 6.

$$T_V = W\cos(\alpha_V) \tag{6}$$

We neglect the horizontal component of the thrust to begin with, since other sources of battery capacity error seem to be greater, such as the effect of the battery pack temperature. The duration of the expected power demand can be deduced from the flight plan. A notional flight plan was used to begin with. Our multirotor use case is analogous to the rover “Structured Driving” case of (Daigle et al. 2016). He states: “We generate a set of structured driving scenarios as follows. First, it is necessary to select a set of waypoints for navigation on the x–y coordinate axes”.

If we neglect the reduction in the hover thrust component due to the tilt of the rotor, we still have an answer that is 95 percent of the actual thrust if the tilt of the rotor disc is less than 20 degrees. The multirotor control system keeps the rotor disk tilt less than 20 degrees for winds less than the operational limit for this project, 15 knots gusting to 20 knots (7.7 m/s to 10.3 m/s), Langley Research Center policy document LPR1720.18. Our 2022 SWS flight campaign noted a flight where the wind operational limit was exceeded and was ended early. It is plotted in Fig. 7. Once we have a load for hovering flight, we can use the reduced-order model that assumes hover energy is a function of vehicle weight and time-of-transit during the hovering flight load. We could account for tilt of the actuator disk due to the effect of horizontal speed and wind to improve the estimate in

future work. We supplemented these simplifying assumptions with direct laboratory measurement of the hover power using one motor and propeller on a test stand instrumented with a force sensor. This was done for one arm of vehicle Aragog (Tarot 18) in our laboratory test range. We located a test done by a drone enthusiast for vehicle Cerf (DJI S1000), (Econfly, 2014). We also did data analysis from various flights of Aragog and Cerf through use of constant altitude segments to approximate the hover power given the vehicle weight.

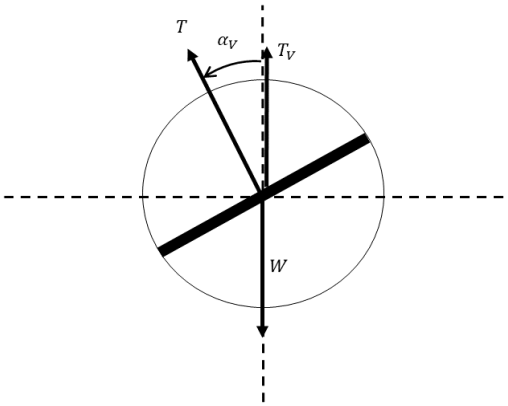

Figure 6. Multirotor vehicle in forward flight free-body diagram.

3.3. Calculation of stochastic charge state variation based on variation of current demand

This section is an outline of how we set the stochastic Gaussian noise inputs. We say stochastic state input variation analysis because we did not perform repeated flight simulations but rather used the hovering nature of the flight to say the flight was a number of segments that were similar to repeating the flight multiple times.

- Assume charge state in coulombs varies proportionately as input current varies.
- Cerf flight F123 was used as a “typical” flight to play back using the electrochemistry model’s four charge state variables and the equivalent circuit model’s two charge state variables.
- A selected value from a run of F123, mid-run was used as “typical” charge magnitude. (28894 C) for the electrochemistry model.

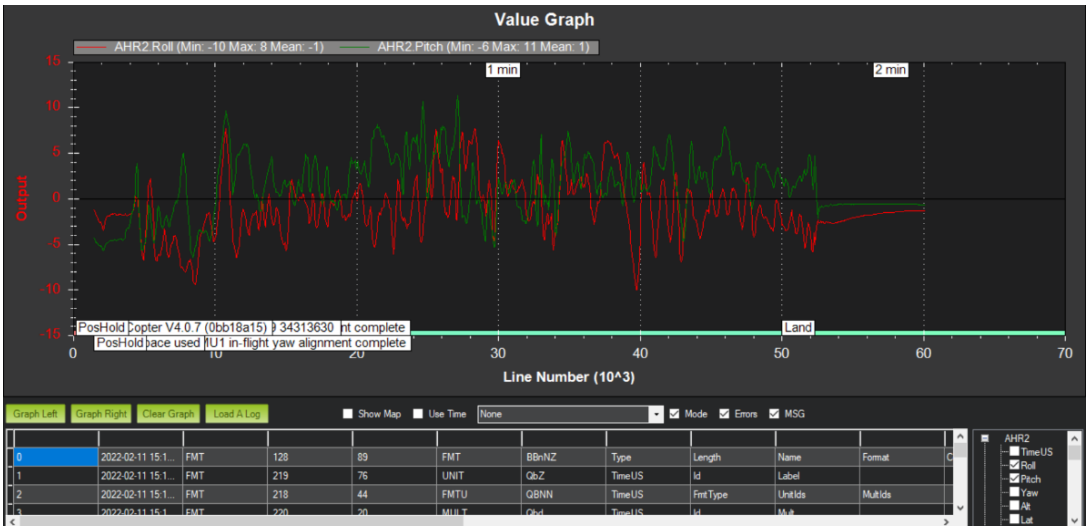

Figure 7. Aragog F056, worst case platform tilt during study, pilot’s wind limit exceeded, roll and pitch excursions less than 20 degrees (Mission Planner playback).

- The input current demand histogram indicated a 57A draw with ±10A three sigma variation if assumed to be Gaussian distribution. This three-sigma variation was reduced to one-sigma variation when analyzing vehicle Aragog because of singularity and stability issues with the electrochemistry model.

3.4. Prediction Uncertainty

The prognostic predictions are affected by different sources of uncertainty. The prediction of the RFT could be considered an uncertainty propagation problem of the battery simulation under future loading conditions. A classification of the sources of uncertainty are:

1. Uncertainty in the present charge state of the battery represented by the state vector $\mathbf{x}(k)$.
2. Uncertainty in the future loading of the battery represented by the set of future loads $\boldsymbol{U}_{\boldsymbol{k_p}} = [\boldsymbol{u}(k_P), \dots, \boldsymbol{u}(k_E)]$, k_P denotes the time when we perform a prediction and k_E denotes the simulated time when the threshold event ending the discharge occurs.
3. Uncertainty in the battery parameters $\boldsymbol{\Theta}_{k_P}[\boldsymbol{\theta}(k_P), \dots, \boldsymbol{\theta}(k_E)]$. In the general case, this would be a set as well; but in our case we assume them to be constant for the duration of the flight.
4. Uncertainty in the process noise $\boldsymbol{V}_{\boldsymbol{k_p}} = [\boldsymbol{v}(k_P), \dots, \boldsymbol{v}(k_E)]$. Also a set in the general case, but we consider it to be white noise with a constant covariance for the duration of the flight.

We add to the simplifying assumption of the battery parameters remaining constant for the flight and that they have been identified offline previously by fitting laboratory discharge experiments. We also make the simplifying assumption that the process noise is small compared to the effect of varying the future flight duration and vehicle weight. This follows the simplifications made by (Daigle et al. 2016).

"Since the system model described […] is an abstraction of this model, there are some actual parameter uncertainties and process noise, but these sources of uncertainty are negligible compared to the future input trajectory uncertainty."

The simplification of the future power demand flows from the power demand characteristics of multirotors that most of the power for the eUAV is expended in a quasi-static hover of the vehicle (Fig. 6). The power to hover a vehicle per rotor is a function of its weight primarily as given by this momentum theory equation (Sierra et al. 2018), (Stepniewski, 1979).

$$P_h = \frac{W^{3/2}}{\sqrt{2\rho A}} \tag{7}$$

Where ρ is air density, and W is the total weight of the vehicle. A is the total disc actuator area, πr^2, where r is the radius of one of eight rotors. According to Fig. 8, that leaves only stochastic variation of the battery current demand due to the engine throttle as it adjusts to wind gusts and mean tilt of the plane of the rotors to compensate for steady winds. The charge state of the battery at the beginning is established through a resting voltage before a flight.

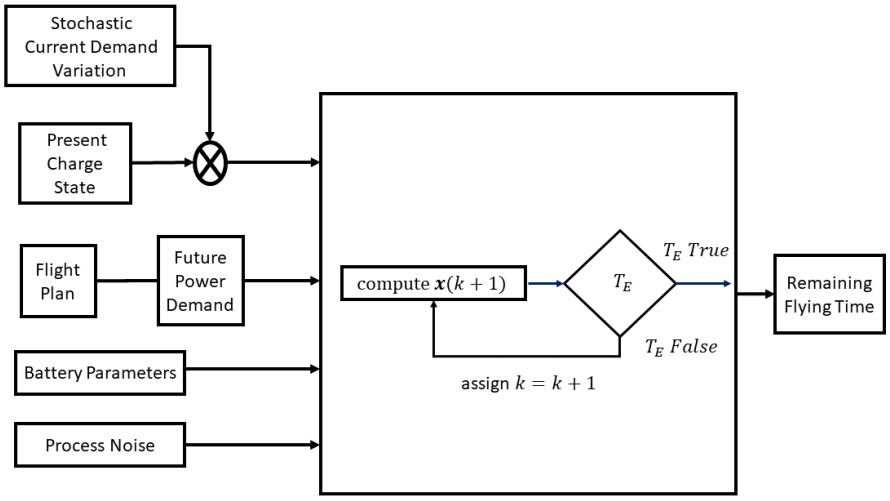

Figure 8. Sources of prediction uncertainty after (Daigle et al. 2018).

In algorithm 1 (Daigle & Sankararaman, 2018) the function R represents the set of predictions that is uncertain

$$R = P(\Xi).$$

A realization of this function R is denoted by

$$\boldsymbol{r} = P(\xi).$$

"…We consider only initial state uncertainty, related to the state estimate obtained by the UKF, and the future input uncertainty. In each experiment, predictions are made every 500 s until the end of discharge (EoD), and the accuracy and precision metrics are averaged over all these predictions" (Daigle et al. 2016).

Algorithm 1. $\mathbf{r} \leftarrow \mathrm{P}(\xi)$

1: $[\boldsymbol{x}(\boldsymbol{k_p}), \boldsymbol{U_{k_p}}, \boldsymbol{\Theta_{k_p}}, \boldsymbol{V_{k_p}}] \leftarrow \boldsymbol{\xi}$
2: $k \leftarrow k_p$
3: $\boldsymbol{x}(k) \leftarrow \boldsymbol{x}(k_p)$
4: while $T_E\left(\boldsymbol{x}(k), \boldsymbol{U_{k_p}}(k), \boldsymbol{\Theta_{k_p}}(k)\right) = false$ do
5: $\quad \boldsymbol{x}(k+1) \leftarrow \boldsymbol{f}(k, \boldsymbol{x}(k), \boldsymbol{U_{k_p}}, \boldsymbol{\Theta_{k_p}}, \boldsymbol{V_{k_p}})$
6: $\quad k \leftarrow k+1$
7: $\quad \boldsymbol{x}(k) \leftarrow \boldsymbol{x}(k+1)$
8: end while
9: $k_E \leftarrow k$
10: $\triangle k \leftarrow k_E - k_p$
11: $\boldsymbol{r} \leftarrow \mathrm{P}([k_E \quad \triangle k_E]^{\boldsymbol{T}})$

4. Equivalent Circuit Model of Battery Capacity (CFS Application "Circ")

This section presents the equivalent circuit battery model. An equivalent circuit battery model is used to represent battery terminal voltage dynamics as a function of the battery current. The model is based on Thévenin's theorem used to model the current and voltage profile of the battery as a black box input-output device. A first-approximation assumption is made such that the battery state can match a linear electrical network consisting of only voltage and current sources and resistances and capacitors. Thévenin states that the black box can be replaced at the input output terminals by an equivalent voltage source in series connection with an equivalent resistance and capacitance. The correspondence of the resistor capacitor (RC) circuit to actual battery chemical phenomena is only notional (Fig. 9). To extend the equivalent circuit model, some of the components were made to vary according to the bulk charge stored in the battery. The SoC is an estimate of the battery bulk charge. The battery input-output voltage dynamics will change as a function of this bulk charge estimate. Figure 10 has the equivalent circuit model proposed by (Daigle et al. 2016) that uses three capacitors. We found (Eure & Hogge, 2021) that the third capacitor (Fig. 10) and the second capacitor caused the battery parameter identification to be not deterministic, and we followed the solution of (Jiang, Wang, Wu, Etse-Dabu, and Xiong, 2020) and removed one of the capacitors (Fig. 11). We used the (Jiang et al. 2020) model merged with the notation of (Daigle et al. 2016). These equivalent circuit model equations are listed in Table 3. The large capacitance C_b holds charge q_b of the battery. The nonlinear C_b captures the open-circuit potential and is a nonlinear function of SoC. The R_{sp} , C_{sp} pair captures the nonlinear voltage drop due to surface

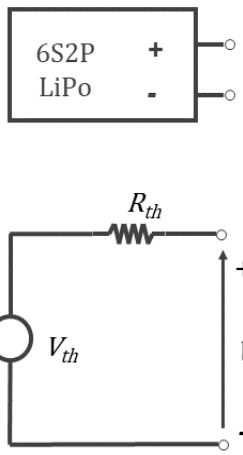

Figure 9. Thévenin equivalent circuit model.

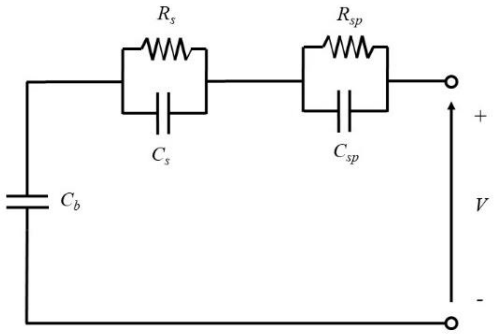

Figure 10. Equivalent circuit model, three capacitors (Daigle et al. 2016).

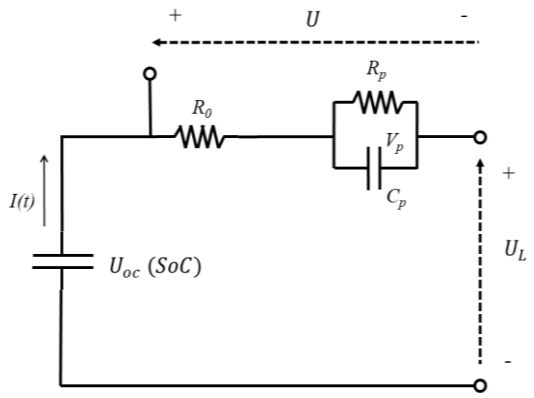

Figure 11. Equivalent circuit model, two capacitors (Jiang et al. 2020).

Table 3. Circ battery model equations.

$$\mathrm{i} = \mathrm{P}/\mathrm{V}$$

$$i_P = 0$$

$$i_b = i$$

$$i_{sp} = i_b - V_{sp}/R_{sp}$$

$$i_s = 0$$

$$V_{sp} = q_{sp}/C_{sp}$$

$$V_s = iR_s$$

$$V = V_b - V_{sp} - V_s$$

$$\dot{q_b} = -i_b$$

$$\dot{q_{sp}} = i_{sp}$$

$$SoC = 1 - \frac{q_{max} - q_b}{C_{max}}$$

$$R_{sp} = R_{sp0} + R_{sp1}\exp\left(R_{sp2}(1 - SoC)\right)$$

$$Cb_0 = \frac{q_0}{V_0}$$

$$Cbp_3 = Cb_0 - (Cbp_0 + Cbp_1 + Cbp_2)$$

$$C_b = Cbp_0 SoC^3 + Cbp_1 SoC^2 + Cbp_2 SoC + Cbp_3$$

overpotential. R_s (Daigle), R_0 (Jiang) captures the ohmic drop. R_{sp} is also a nonlinear function of SoC. The model is implemented as a discrete-time version with a time step of one second. One additional equation, Fig. 12, presents the SoE as the ratio of the residual available energy to the maximum available energy. In our case this can be thought of as the SoC which is scaled by a gain of the model voltage output V, V_m scaled by V_0 (the initial voltage of the battery at rest before take-off).

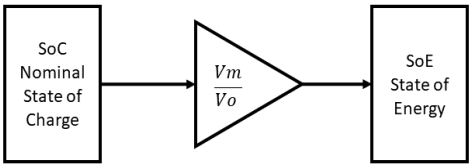

Figure 12. State of energy (SoE) for the Circ and Chem models.

5. Basic Electrochemistry Model of Battery Capacity (CFS Application "Chem")

The purpose of this section is to present a simplified electrochemistry model. The complete model is found in (Daigle et al. 2013b) and described in Appendix A. The parameters $q_{s,p}(k)$, $q_{s,n}(k)$ are the mobile lithium ions at the positive and negative electrode surface at model discrete time step k with a sampling period of Δt. The current flow into and out of the battery terminals is i. In Eq. set (8), R is the universal gas constant, n is the number of electrons transferred in the cell reaction, T is the electrode temperature, and F is Faraday's constant.

A simple model of an ideal electrochemical cell at equilibrium is the Nernst equation shown as the third and fourth equations in in Eq. set (8) for $V_{U,p}$ and for $V_{U,n}$. These are the terminal voltages for an ideal battery which are not directly used for battery modeling since they are only valid for equilibrium conditions, unlike the conditions present for a cell under load. They are important for basic understanding, nevertheless. For a cell under load, we need to model the battery dynamics. The Nernst equation Eq. set (8) is coupled with the Redlich-Kister expansion as shown in Eq. set (9) (Redlich & Kister, 1948), (Karthikeyan, Sikha, & White, 2008), to approximate the non-ideal battery behavior. The physical meaning of each parameter is the same as given in (Daigle et al. 2013b), (Daigle, 2016a) and also reviewed in Appendix A. The Chem battery model is a simplified model that begins to adhere to basic chemistry and physical principles. A summary of the constants and the variables to be identified by a Nelder-Mead fit of a low-current discharge is presented in Table 7. The model is implemented as a discrete-time version with a time step of one second.

$$q_{s,p}(k) = q_{s,p}(k-1) + i(k-1)\Delta t$$

$$q_{s,n}(k) = q_{s,n}(k-1) - i(\mathrm{k}-1)\Delta \mathrm{t})$$

$$V_{U,p} = U_{o,p} + \frac{RT}{nF}\ln\left(\frac{q_{sMax} - q_{s,p}}{q_{s,p}}\right)$$

$$V_{U,n} = U_{o,n} + \frac{RT}{nF}\ln\left(\frac{q_{sMax} - q_{s,n}}{q_{s,n}}\right)$$

$$V = V_{U,p} - V_{U,n}$$

$$SoC = \frac{q_{s,n}}{0.6q_{max}} \quad (8)$$

Although more complex, the electrochemistry model parameters can be fit to closely match the battery dynamics. However, this complexity and precision sacrifices robustness. The simpler models are less precise but are more forgiving of errors in the model parameters.

$$x_{s,p} = q_{s,p}/q_{sMax}$$

$$x_{s,n} = q_{s,n}/q_{sMax}$$

$$V_{INT,p} = \frac{1}{nF}\sum_{j=0}^{N_p} A_{p,j}\left(\left(2x_{s,p}-1\right)^{j+1} - \frac{2x_{s,p}j\left(1-x_{s,p}\right)}{\left(2x_{s,p}-1\right)^{1-j}}\right)$$

$$V_{INT,n} = \frac{1}{nF}\sum_{j=0}^{N_n} A_{n,j}\left(\left(2x_{s,n}-1\right)^{j+1} - \frac{2x_{s,n}j\left(1-x_{s,n}\right)}{\left(2x_{s,n}-1\right)^{1-j}}\right)$$

$$V_{U,p} = U_{0,p} + \frac{RT}{nF}\ln\left(\frac{1-x_{s,p}}{x_{s,p}}\right) + V_{INT,p}$$

$$V_{U,n} = U_{0,n} + \frac{RT}{nF}\ln\left(\frac{1-x_{s,n}}{x_{s,n}}\right) + V_{INT,n}$$

$$V = V_{U,p} - V_{U,n} \quad (9)$$

6. Comparison of the two models

6.1. Fitting to flight test results

To assess the performance of the battery models there were a few conditions that could be easily tested. The relationship between the voltage at equilibrium of the battery and the SoC is given through a quasi-static discharge where the battery remains at ambient temperature and few intermediate products of the cell reactions accumulate in the bulk electrolyte. See Fig. 16 and Fig. 17 for an example discharge profile of a typical battery used by our multirotors. With this relationship we can compare the model estimated SoC at landing with the SoC read from the discharge graphs based on the resting voltage present 60 minutes after landing. We also can use the model estimated end of discharge (EoD) or RFT compared to the actual flying time. We can compare the landing SoC with that looked up from the equilibrium SoC graph to estimate the remaining flying time remaining at landing if the flight had continued to EoD. The modeled voltage should match the measured voltage if the model is working well. Another ground truth not used in this work is an estimate of the battery's internal resistance from the take-off loading. This could be used to compare the model fitted internal resistance value in the future.

The Circ and Chem models were each fitted to laboratory battery discharge data. The Nelder-Mead algorithm selected the set of battery parameters with the lowest least squares error. This algorithm is a simplex gradient descent and implemented by the MATLAB *fminsearch* function. The discharge data fitted was the result of laboratory experiments performed by an automatic battery cycler that produced the discharge data profiles. Each model required compromises in the tuning to prevent oscillation (instability) of the modeled voltage estimates and oscillation of the SoC estimates. We found that a reduction in the order of the models made the fit more deterministic. We reduced the number of capacitors in the Circ model to produce a more robust model. This resulted

in a model similar to Fig. 11 by (Jiang et al. 2020) instead of the model from our earlier work shown in Fig. 10. We mapped the variable names from the Jaing, Fig. 11, model to the Daigle, Fig 10, model. This results in Jaing R_0 becoming Daigle R_s, Daigle C_s constrained to be zero, and Jaing R_p and C_p becoming Daigle R_{sp} and C_{sp}. Thus, the Table 3 Circ model still holds with the Jaing diagram with this mapping.

6.2. Tuning of models to match measured and model estimated voltage

Another problem encountered was that the model estimated voltage differed from the actual voltage in the flight data. There seemed to be a nonlinear temperature dependence, see section 8.1. We attempted to close this difference through tuning of flights with similar conditions. We used typical flights to serve as reference flights for tuning the discharge response of vehicle Aragog (Tarot 18) and the Vehicle Cerf (DJI-S1000). Specifically, Aragog flight 98 and Cerf flight 123 were used. The following is an outline of the tuning process.

- Perform a playback of the data from the day of the flight and configure the termination SoC threshold of the playback flight value to be close to the value derived from the rest voltage 20 minutes after landing or that from one hour after landing depending upon availability. Use the rest voltage value to select a corresponding SoC value from the laboratory low current (1/50 C) discharge profile.
- Determine the time of takeoff and landing using output files from the autopilot logs and the CFS logs of altitude and current demand.
- Use hover VI power demand (the product of voltage V and current I) to calculate an electrical power to mechanical power efficiency factor according to the aerodynamic momentum theory equation Eq. (7).
- Use a flight with a deep discharge to tune the EoD estimate to match the actual landing time, accounting for the flying time remaining as if the SoC limit threshold had been achieved through extrapolation. Figure 14 has an 8 second moving average applied to the estimates and a quiet tuning magnitude of noise added to the model internal charge states. Figure 15 has no averaging and the full one standard deviation (1 σ) of noise added to the charge states.
- Because of a mismatch in the modeled voltage to the actual measured voltage of both models Circ and Chem under full hovering load, we needed to use an empirical coefficient to set the estimated voltage under load to approximate the actual voltage under load Fig. 13. (More on this under temperature dependence of the models, section 8.1)
- Also, in an effort to keep similar SoC discharge profiles, Fig. 13, and EoD estimates, Fig. 14 and 15, we use an empirical process to bias the initial model charge states to be larger than the fitted charge states based on the laboratory discharge experiments in order to allow the models to reach the deepest discharge state without running out of charge. The Circ model uses the process described by Daigle, (2016b). "If C_b was linear then: $C_b = q_d/V_d$; but C_b is not linear so guessing that initial charge is more than q_d, it must be large enough such that $C_{bEnd} > C_{b0}$ ". We adapted a similar process he used for the Circ model. We also adapted the process to the Chem model, except more charge states needed to be manipulated.

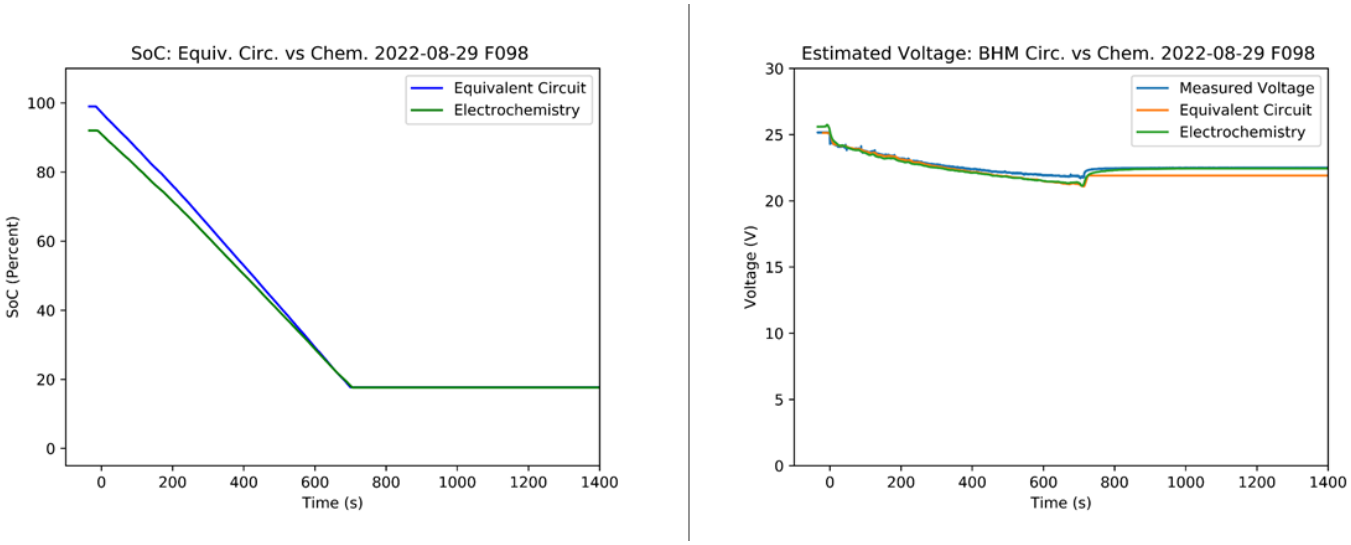

Figure 13. SoC and modeled voltage Circ and Chem, quiet tuning, vehicle Aragog F098.

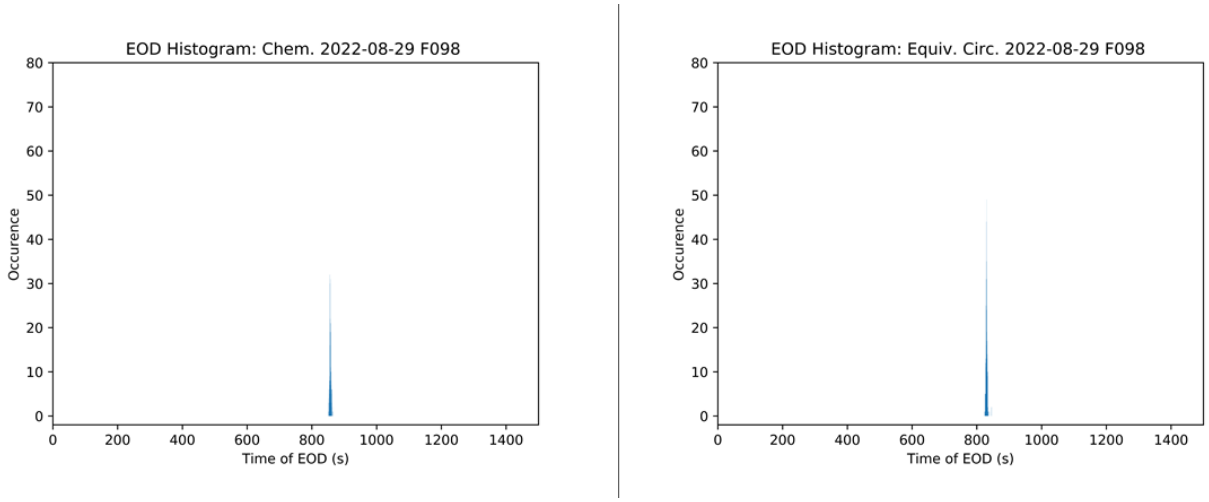

Figure 14. EoD, quiet tuning 8 second. moving average, models Circ and Chem, vehicle Aragog F098.

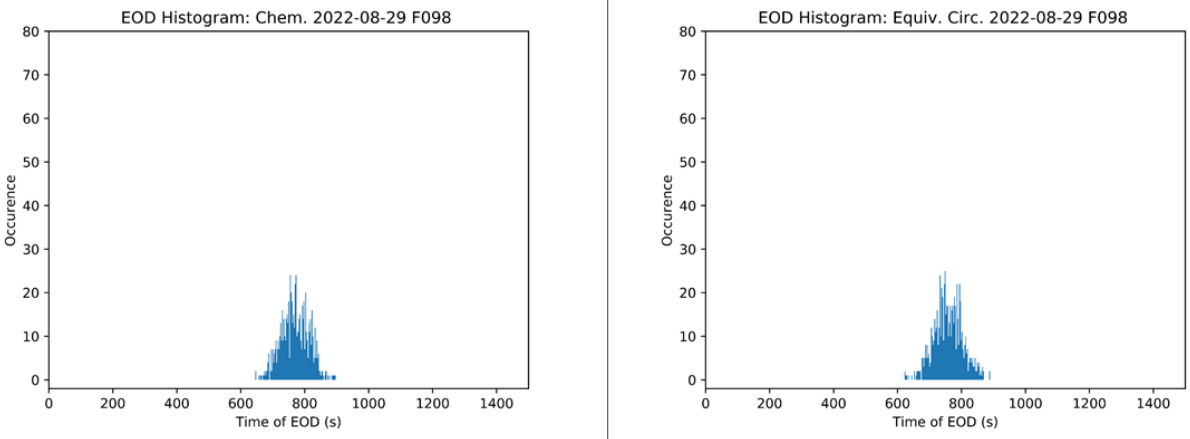

Figure 15. EoD, 1 σ tuning Circ and Chem, vehicle Aragog F098.

7. Battery Model Parameter Identification

The purpose of this section is to outline the methods used in identifying model parameters. Three sets of data will be used to identify the battery model variables. The first set was obtained by slowly discharging a fully charged battery and measuring the current and voltage (1/50 C). The second set was obtained based on a one-C discharge (one-C meaning that a fully charged battery rated at 1Ah should provide 1 ampere for one hour). The third set was obtained using a variable current discharge of a magnitude that would approximate multirotor operations. In all cases the battery voltage and current were recorded at a sampling rate of one hertz. Identification was performed in MATLAB using a Nelder-Mead downhill simplex method solution search *fminsearch* that minimizes the error between the modeled and actual voltage profile. This section provides some information about the ordering of identification steps and plots demonstrating the quality of model fit for the training data.

7.1.Identification of Equivalent Circuit Model Parameters

The equivalent circuit battery model contains electrical components and empirical equations that are tuned to recreate the observed current-voltage dynamics of the battery. These battery parameters were identified by fitting a pulsed discharge laboratory experiment voltage profile with a Nelder-Mead solution search. These identified parameters are associated with a selected battery from a batch of batteries of a given chemical formulation. These parameters are assumed to be unvaried across all similar battery packs of a given batch. Any differences in individual batteries due to manufacturing variation are accounted for by adaptation of the battery charge capacity term C_{max} of the C_b capacitor in the equivalent circuit model.

A second laboratory fitting experiment to identify C_{max} is run by performing a 1/50 C slow discharge cycle for each battery. During this low current discharge cycle, the voltage across the C_b capacitor plays a dominant role. Thus, this experiment allows the C_{max} parameter to be fitted in isolation. Model parameters are found for the first-

order model of the equation set in Table 3 using the slow discharge data set. To initialize these variables, information about the battery pack is obtained from the manufacturer to initialize the Nelder-Mead solution search. Initialization is performed as shown below and the first set of model current parameters is listed in Table 4. Here V_0 is found by averaging the first ten voltage readings at the beginning of the discharge, C_{max} is the integral of the entire current history needed to discharge the battery, and q_{max} is set slightly larger than C_{max} in order to ensure SoC does not exceed one.

$$C_{max} = \int idt$$

$$q_{max} = 1.02C_{max}$$

$$C_b = \frac{q_{max}}{V_0}$$

$$V_0 = mean\big(V(1{:}10)\big)$$

The data is run back through the resulting model to ensure a reasonable fit. The resulting output voltage and SoC estimation are shown in Fig. 16 and Fig. 17. As can be seen in the figures, the resulting model closely approximates battery behavior for the slow discharge case. We see that the measured and estimated voltages are similar, and that the SoC goes from fully charged (1.0) to fully discharged (0.0).

When the equivalent circuit model is extended to include an additional state, the original parameters from the first-order model are held constant and the additional parameters are identified using the one-C discharge data. Here the second-order model is that of Eq. set (10). The

Table 4. First-order model Circ parameters for battery D027.

Parameter	*fminsearch* Result
C_{bp0}	570.015 F
C_{bp1}	261.205 F
C_{bp2}	3477.205 F

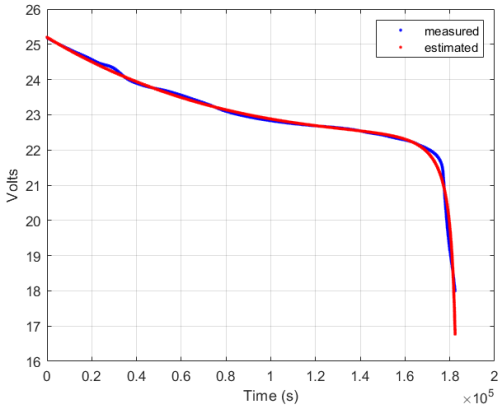

Figure 16. First-order Circ battery voltage.

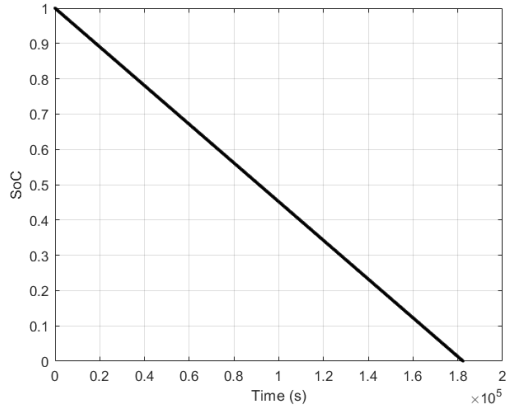

Figure 17. First-order Circ state of charge.

parameters to be identified are shown in Table 5. As with the first-order model, the second-order model is checked with the data used for model identification to see if the fit is reasonable. The plots are shown in Fig. 18 and Fig. 19.

Table 5. Second-order Circ battery parameters for battery D027.

Parameter	*fminsearch* Result
C_{sp}	1608.1265 F
R_{sp0}	0.000000 Ω
R_{sp0}	0.001947 Ω
R_{sp0}	0.020000 Ω

$$q_b(k) = q_b(k-1) + i(k)\Delta t = f_1$$

$$q_{sp}(k) = \exp\left(\frac{-\Delta t}{C_{sp}R_{sp}}\right) q_{sp}(k-1) + C_{sp}R_{sp}(t)\left(1 - exp\left(\frac{-\Delta t}{C_{sp}R_{sp}(k)}\right)\right) = f_2$$

$$SoC = 1 - \frac{q_{max} - q_b(k)}{C_{max}}$$

$$R_{sp}(\mathrm{k}) = R_{sp0} + R_{sp1}\exp(1 - SoC(k))$$

$$C_b(k) = Cbp_0 SoC(k)^3 + Cbp_1 SoC(k)^2 + Cbp_2 SoC(k) + Cbp_3$$

$$V(k) = \frac{q_b(k)}{C_b} + \frac{q_{sp}(k)}{C_{sp}} \quad (10)$$

In battery D027 there seems to be a zone of instability between measured one-C discharge profile with the modeled voltage profile on the line or above the one-C discharge measured voltage line, and 1/2 volts below the one-C line. Battery D004 was able to be stable at the line but D027 was not. We distorted the D004 fit by increasing the R_o constraint to better match D027 but at the expense of the Step 3 variable load fit being biased.

The third-order battery model is presented next. The additional parameters are shown in Table 6. In determining the parameter values, a variable discharge was used. As with the first and second-order system, the fit is reasonable; see Figs. 20 and 21.

Table 6. Third-order model Circ battery parameters.

Parameter	*fminsearch* Result
R_s	0.015 Ω

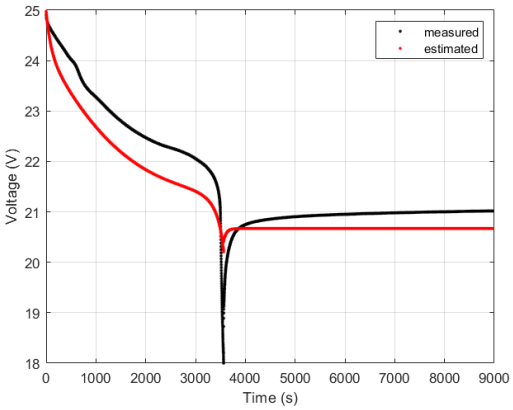

Figure 18. Second-order Circ battery voltage.

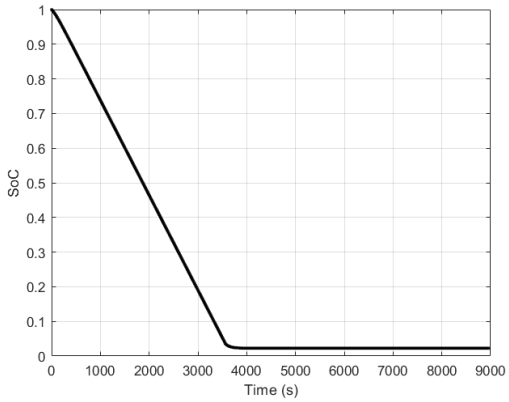

Figure 19. Second-order Circ state of charge.

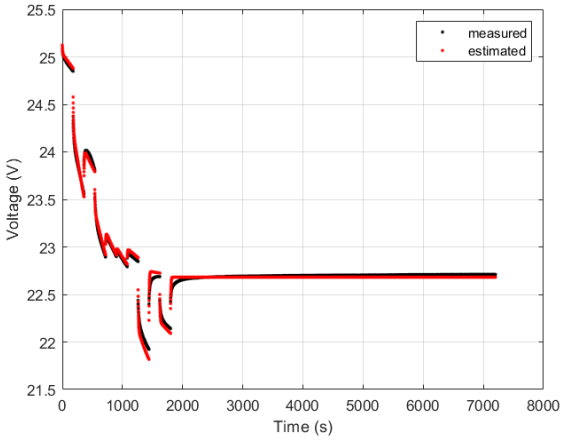

Figure 20. Third-order Circ battery voltage.

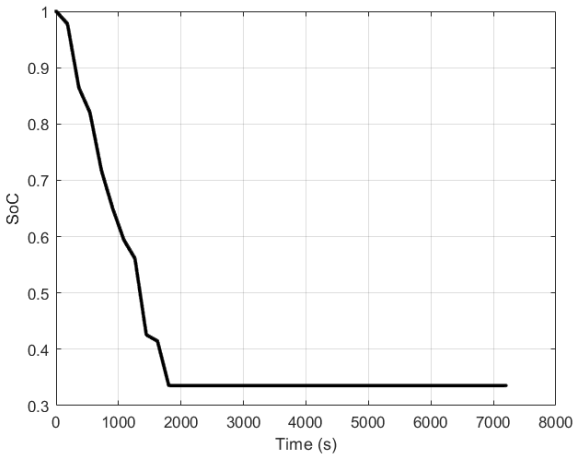

Figure 21. Third-order Circ state of charge.

7.2. Identification of Electrochemistry Model Parameters

In this section we consider the identification of the electrochemistry model parameters as shown in Eq. set (9). The electrochemistry model is described in Appendix A. There is a more detailed description of the electrochemistry model in (Daigle et al. 2013b). Parameter identification is a three-step process using a slow discharge data set, a one-C discharge data set, and a variable discharge data set. This electrochemistry model is based on the Nernst equation shown in Eq. set (8). In an ideal battery at equilibrium, the potential of an electrode is given by the Nernst equation, the positive electrode, for example:

$$V_{U,p} = U_o + \frac{RT}{nF}\ln\left(\frac{\gamma_{\beta,p}\, x_{\beta,p}}{\gamma_{\alpha,p}\, x_{\alpha,p}}\right), \tag{11}$$

rewriting the Nernst equation using logarithm's properties,

$$V_{U,p} = U_o + \frac{RT}{nF}\ln\left(\frac{x_{\beta,p}}{x_{\alpha,p}}\right) + \frac{RT}{nF}\ln\left(\frac{\gamma_{\beta,p}}{\gamma_{\alpha,p}}\right), \tag{12}$$

where U_o is a reference potential, R is the perfect gas constant in joules/mole/kelvins, T is the electrode temperature in kelvins, n is the number of electrons transferred in the reaction ($n = 1$ for Li-ion). F is Faraday's constant, x is the mole fraction, the α subscript refers to the lithium-intercalated host material and the β subscript to the unoccupied host material. In an ideal condition the last term of Eq. 11 disappears leaving the classical form of the Nernst equation (Daigle et al. 2013b).

The expression that is the argument of the natural logarithm is a ratio of the oxidation and reduction reactions' activities α. γ is the activity coefficient that accounts for the non-ideal behavior of real solutions (page 184, Atkins et al. 2018).

$$\frac{a_\beta}{a_\alpha} = \frac{\gamma_{\beta,p}\, x_{\beta,p}}{\gamma_{\alpha,p}\, x_{\alpha,p}}$$

In the case of a Li-ion battery, $x_\beta = 1 - x_\alpha$. We rewrite the equation using

$$x_p = \frac{q_p}{q_{max}}$$

where q_{max} is the sum of the positive and negative Li ions as given by Eq. A.15.

We make the substitution into the second term of Eq. 11 and rename the third term to be $V_{INT,p}$ where $V_{INT,p}$ is the activity correction term for the nonideal condition.

$$V_{U,p} = U_o + \frac{RT}{nF}\ln\left(\frac{1 - x_p}{x_p}\right) + V_{INT,p} \tag{13}$$

$V_{INT,p}$ is given by the Redlich-Kister expansion introduced in Eq. set 9, (Redlich et al. 1948), (Karthikeyan et al. 2008).

$$V_{INTp} = \frac{1}{nF}\sum_{j=0}^{N_p} A_{p,j}\left(\left(2x_{s,p} - 1\right)^{j+1} - \frac{2x_{s,p}\, j\left(1 - x_{s,p}\right)}{\left(2x_{s,p} - 1\right)^{1-j}}\right) \tag{14}$$

The $2x_{s,p} - 1$ denominator term causes problems when near zero and will be discussed in section 8.2. This series expansion is a Padé approximate, (section 5.12 Press, Teukolsky, Vetterling and Flannery, 1996). The reference cautions that the approximation equations are

frequently close to singular and gives guidance on solution approaches.

Figure 22 shows the ability of the electrochemistry model to track the measured battery voltage and estimate the SoC. Performance is like the equivalent circuit model as shown in Fig. 16. After the values of Table 7 are determined using the Nelder-Mead search based on equations A.21 and A.22 and the slow discharge data set, the remaining variables of the full electrochemical model of reference (Daigle et al. 2013b) may be used to find the remaining values by using the one-C discharge data. These values are shown in Table 8. The variable current data set is used to verify operation of the full electrochemistry model as shown in Fig. 23 and Fig. 24.

Table 7. First-order battery parameters for Chem model.

Parameter	*fminsearch* Result
q_{max}	1.5644e+05
$U_{0,p}$	2.3958e+01
$U_{0,n}$	5.3950e-02
$A_{n,0}$	8.3795e+02
$A_{p,0}$	-3.5945e+05
$A_{p,1\ldots7}$	6.0598e-01
	1.2516e+05
	-5.1572e+05
	-1.0277e+05
	2.5112e+06
	2.7440e+05
	-9.6805e+06

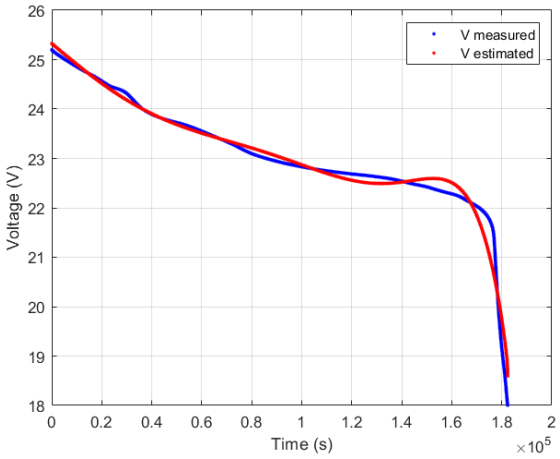

Figure 22. First-order Chem battery voltage.

Table 8. Second and Third-order battery parameters for Chem model.

Parameter	*fminsearch* Result
$t_{Diffusion}$	1.2793e+06
R_0	1.7270e-02
τ_0	1.4711e+01
$\tau_{\eta,p}$	2.7921e+01
k_p	1.7408e+01
$\tau_{\eta,n}$	6.0357e+05
k_n	5.5396e+06

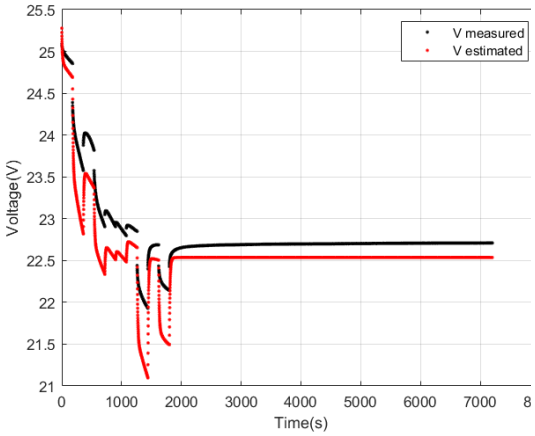

Figure 23. Third-order Chem battery voltage.

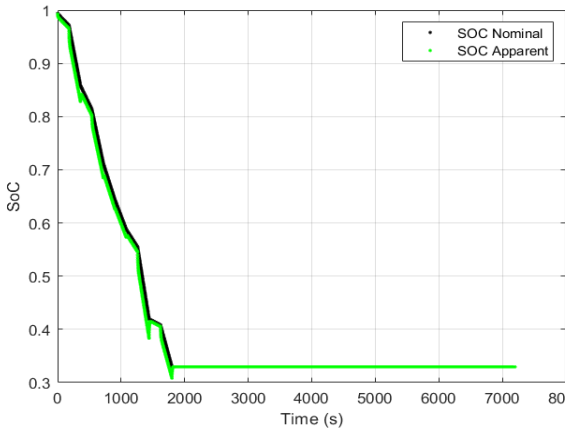

Figure 24. Third-order Chem state of charge.

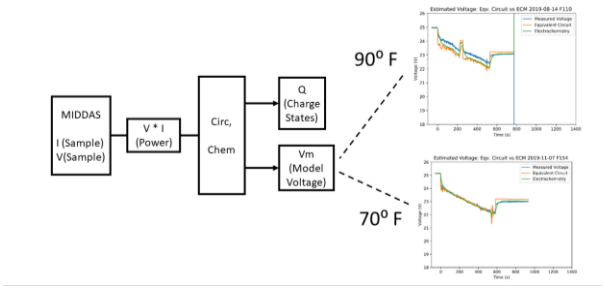

Figure 25. Battery voltage unmodeled temperature variation during 2019 campaign, Cerf DJI S1000.

8. Lessons Learned, Testing experience

8.1. Unmodeled Temperature Dependence of Modeled Voltage in both Chem and Circ.

In this section we examine the influence of the ambient temperature on the modeled voltage of the battery as compared with the measured voltage during operation. During the 2019 flight campaign using vehicle Cerf, we noticed a temperature effect (Fig. 25). We later tried to adjust for the temperature effect. The modeled voltage was initially derived from the laboratory discharge experiment run at room temperature. The various flights of the System-Wide Safety flight campaign took place various times of the calendar year. Some were run during hot conditions in the summer. Some were run in cold conditions in the winter and in between. When the ambient conditions were close to the laboratory's room temperature the model voltage matched the measured voltage the closest. We used empirical factors to bias the load and the initial charge condition to bring together the modeled and measured battery voltage for a flight group during warm days, cool days, etc. We added an outer loop tuning coefficient for the estimated voltage. We used the deep-discharge flight 98 (Fig. 26 and Fig. 27) to tune the warm day flights for vehicle Aragog. Both models Chem and Circ had voltage displacement issues when the battery temperature differed from the laboratory temperature when we made the battery characterization runs. Model Circ had this dependence even though there was no explicit temperature dependence in its equivalent circuit model.

The temperature dependence of model Chem did not account for the deviation of the estimated voltage from the ambient temperature either. The temperature profile of Fig. 26 began around 88 degrees F and increased approximately linearly to 109 degrees F at the time of landing. We adjusted the estimated voltage for both models to approximately agree with the measured voltage under load. The Chem model was adjusted to match the recovery period voltage. The Circ model estimated voltage did not recover to the post-flight resting voltage. The Circ model requires current in order to make a voltage estimate and the estimated voltage during the recovery period is not observable (Eure et al. 2020). The Aragog flight 117 battery temperature was cooler than the temperature when the characterization data was recorded. It overestimated the voltage (Fig 28. and Fig. 29) at the beginning of the flight. The ambient temperature was 66 degrees F. The estimated voltage tuning was done using the factors from Aragog

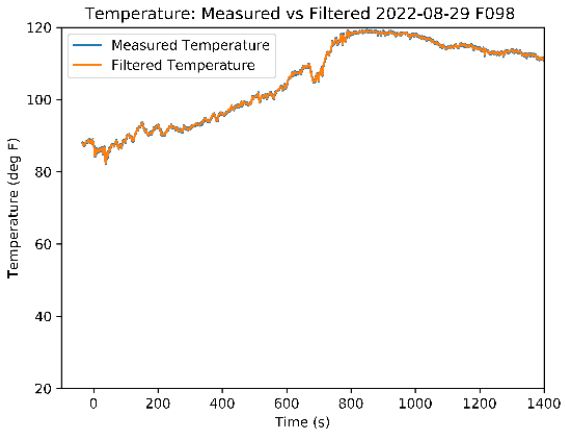

Figure 26. Warm-day measured temperature, Aragog T18 flight 98.

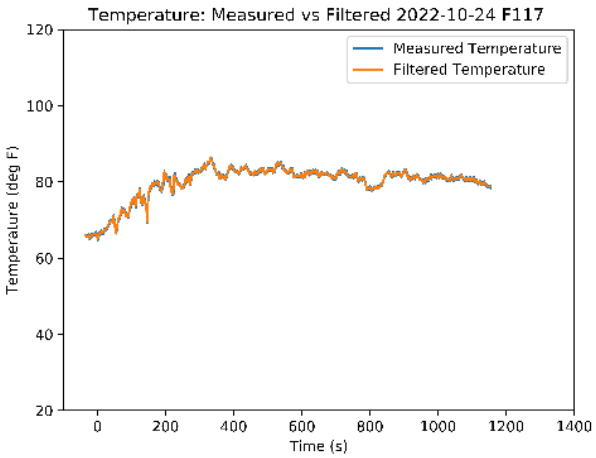

Figure 28. Aragog cool-day measured temperature flight 117.

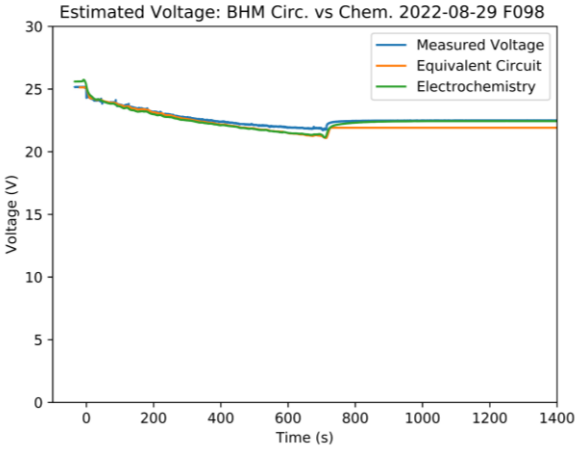

Figure 27. Measured and modeled voltage, flight 98, warm-day tuning, Aragog flight 98.

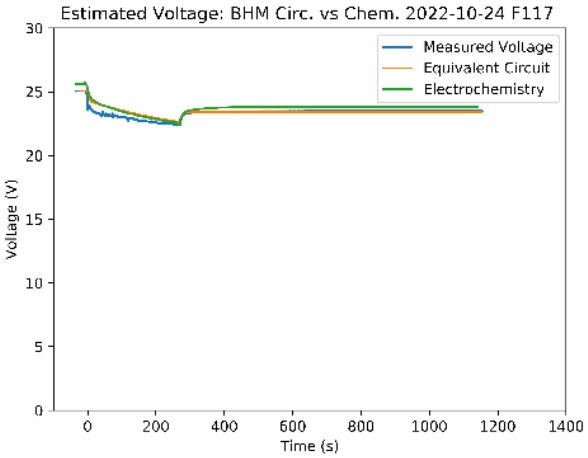

Figure 29. Aragog cool-day measured and modeled voltage flight 117.

flight 98 done on a warmer day (86 degrees F). Aragog flights 92, 94 and 101 estimated the voltage well. It seems that flights with an ambient temperature of 70 degrees F and higher perform similarly to laboratory discharges if tuned to the laboratory conditions only, but runs with the ambient temperature under 70 degrees F tend to overestimate voltage.

8.2. Constraints were added to the battery parameter identification to avoid various instabilities in both Chem and Circ.

We identified a singular condition in the Chem equations in the overpotential calculation, Eq. A21, and in the Redlich-Kister equilibrium potential calculation, Eq. A.22, (Redlich & Kister, 1948), (Karthikeyan, Sikha, and White, 2008). Terms dependent upon the ion concentration at the surface of the electrodes trended too close to zero in the denominator of one equation and in the argument of a logarithm function. The battery discharge simulations had stepped the singular region, but occasionally came too close which broke the model. We did a work-around solution that tested the terms for closeness to zero (a singular point) and decided not to calculate the result there but instead to use the answers from previous steps (modeled voltage values). These tests

increased robustness, and the tests facilitated better identification of the battery parameters. An alternative approach may be possible (see Tomiska, 1984).

A zero-current input condition is not observable and sensor parameter variation can excite model instabilities, (Eure et al. 2020). The model input needs to be screened to avoid negative current values and needs to be screened to avoid input of the large positive and large magnitude negative values into the model. Collection of additional data exposed the models to a more diverse data set and uncovered cases where the model with the identified parameters were near a feedback condition. The time response of the models was slowed by bounding the time constants and internal resistance to avoid exciting computational instability.

9. Results

We look at the extent the data is normally distributed (Gaussian) that would allow confidence-interval estimates of the population parameters through parametric estimation methods. In our case the nonlinearity of the estimates at their extreme values pointed to the use of non-parametric (rank) estimation methods. We ended up characterizing the distributions through the use of box plots and histograms as an attempt to describe the diversity of the observed data.

9.1. Vehicle Cerf cool day flights

In Fig. 30 the variation in the current for the day with 13 mph winds as measured by nearby Langley Air Force Base seems to be tilted to the higher current and distorted from a Gaussian shape. The current for the day with half the wind (6 mph) seems more symmetric. However, both of the End of Discharge (EoD) distributions seem very similar regardless of the wind variation. The three-sigma red arrow is given to show what three standard deviation variation of the charge states for Cerf looks like at the histogram scale. We next consider the input current variation and the input voltage variation since these are related to the internal states of model Chem. We used a quantile-quantile plot to assess the degree that our distributions compared to a Gaussian distribution. The plot is called a normal probability plot when the Gaussian distribution is considered the ideal distribution for comparison to the data set (page 225, Hoaglin, Mosteller, and Tukey, 1983). Based on the shape of the normal probability plot, we can classify the distribution as compared with a Gaussian distribution. In the rightmost plot of Fig. 31, the Quantile-Quantile plot of the current fits the pattern of a Heavy-tailed distribution at the extremes, but closer to a normal distribution in the center. In a similar manner we consider the variation of the voltage states high-pass filtered and presented in a normal probability plot to likewise fit the pattern of a heavy-tailed distribution at the extremes, but closer to normal at the center of the Quantile-Quantile plot of Fig. 32. A distribution that is heavier tailed than a Gaussian may be the result of sampling from a mixture of two Gaussian distributions with equal means but unequal variances (page 227, Hoaglin et al. 1983).

The estimate of EoD by the Chem model for vehicle Cerf flight 123 was analyzed through comparison of the residuals with a Gaussian distribution as was done with the current and with the voltage in Fig. 33. In this case the normal probability plot fits the pattern of a light-tailed distribution. The extremes seem closer to Gaussian than the extremes of either the current (Fig. 31) or the voltage (Fig. 32) inputs. A mixture of Gaussian distributions with identical variances but different means may be light tailed (page 350, Hoaglin et al. 1983). This would indicate that the model is a more robust estimator than the heavy-tail current and voltage inputs would imply.

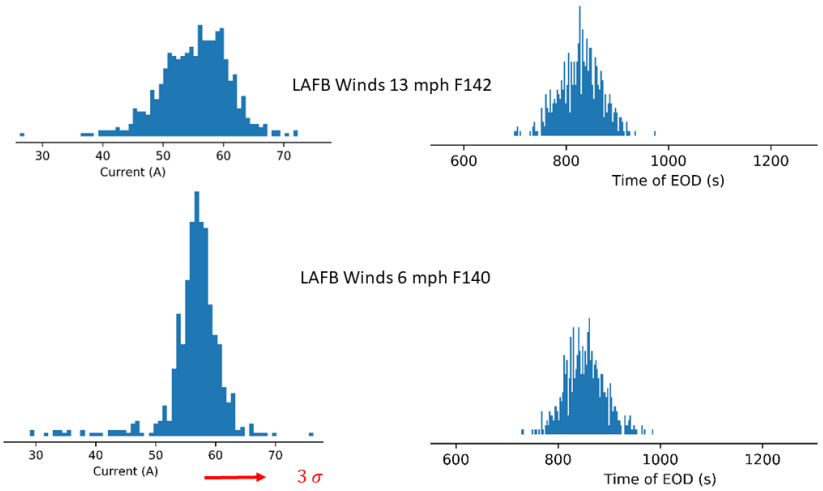

Figure 30. Flying time variation with wind speed vehicle Cerf, EoD from Chem model.

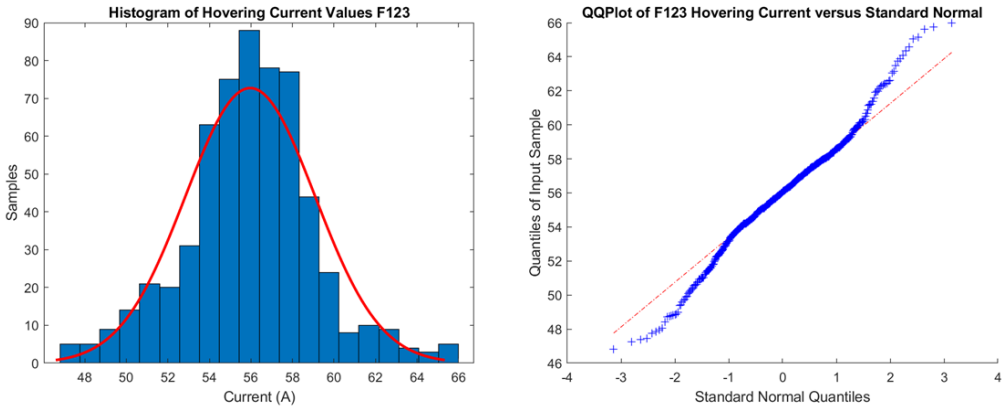

Figure 31. Cerf flight 123, variation of current approximately Gaussian (heavy tailed).

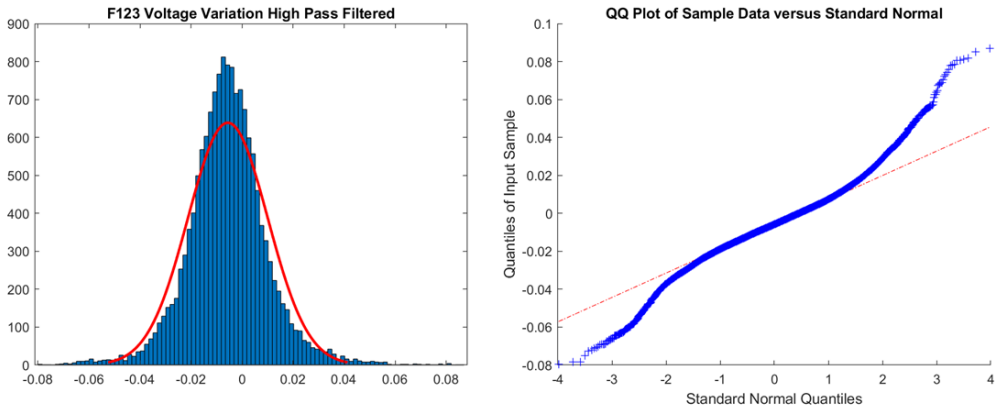

Figure 32. Cerf flight 123, variation of high pass filtered voltage approximately Gaussian (heavy tailed).

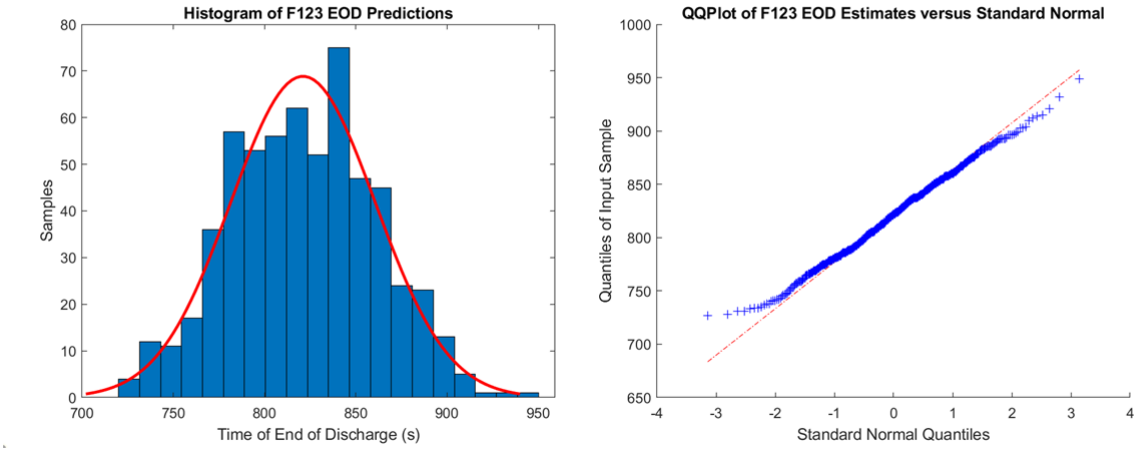

Figure 33. Cerf flight 123, variation of EoD approximately Gaussian (light tailed).

9.2. Performance of the battery model SoE estimate at landing with quiet input tuning, 8 second moving average (flight configuration)

We now describe our process of capturing the variation in the remaining flying time (RFT) and EoD estimate by using the quiet stochastic model state variation with an 8-second moving average filter. Table 9 has the values of the box plots shown in Fig. 34. Likewise, Table 10 has the box plots shown in Fig. 35. We first look at the distributions indicated by the box plots of the Circ and Chem models for

Table 9. Box plot distribution values, SoE difference from truth: 7 Cerf DJI S1000 flights, quiet tuning, 8-second moving average.

Box plot value	Chem	Circ
minimum	-5.7300	-4.5402
median	-3.5354	-0.0955
maximum	10.6415	12.9386
lower fourth (quartile)	-4.3637	-1.4346
upper fourth (quartile)	0.1467	3.1764
IQR	4.5104	4.6111
$\mu\ (mean)$	-1.0083	1.6838
$\sigma\ (std.dev.)$	5.2602	5.4395

Table 10. Box plot distribution values, SoE difference from truth: 5 Aragog T18 short flights, quiet tuning, 8-second moving average.

Box plot value	Chem	Circ
minimum	-8.9778	-2.6067
median	-8.5098	-1.9873
maximum	-1.7552	1.2255
lower fourth (quartile)	-8.5792	-2.0051
upper fourth (quartile)	-4.1433	-0.9081
IQR	4.4358	1.0970
$\mu\ (mean)$	-6.3931	-1.2564
$\sigma\ (std.dev.)$	2.9159	1.3564

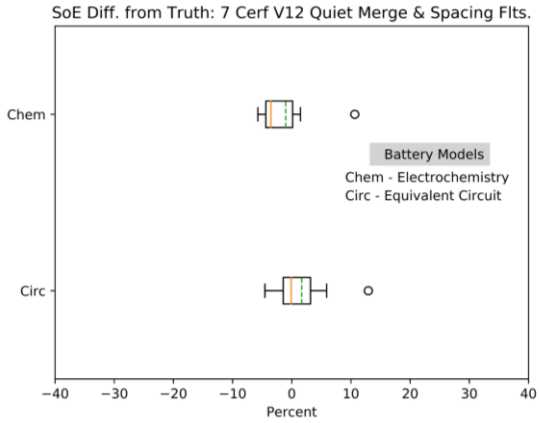

Figure 34. SoE difference from truth: 7 Cerf DJI S1000 flights, quiet tuning, 8-second moving average, mean value is dashed green line.

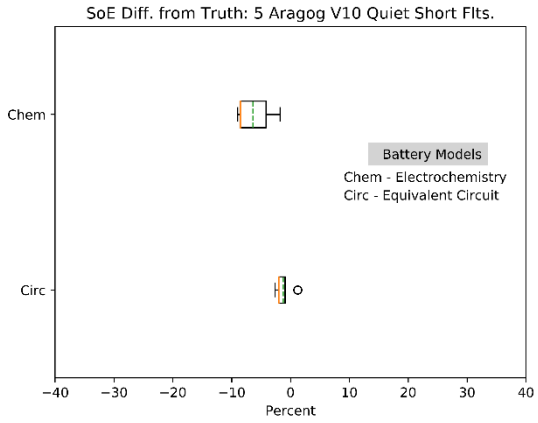

Figure 35. SoE difference from truth: 5 Aragog T18 short flights, quiet tuning, 8-second moving average, mean value is dashed green line.

vehicle Cerf (DJI S1000) that have an eight-step moving average and an input noise tuned to be quiet enough to allow the RFT and EoD estimates to be stable and suitable for filling the display to guide the operator. The Fig. 34 box plots both seem to be skewed to the right based on inspection of the maximum and minimum limits and the relative locations of the median and mean values. If the median and mean lines were collocated it would imply a normal (Gaussian) distribution. However, this distribution is skewed to the right, indicating a possible underlying nonlinearity. The box plots from the short Aragog (T-18) flights using the same two battery models have a similar distribution, with the Circ model of Aragog being more clustered about the median. The Fig. 35 distribution is similarly skewed to the right, but without the large outlier of more than 10 percent seen in the Fig. 34 plots. The reason we compare the Cerf flights with the Aragog selected shorter flights is that these are comparable with the Cerf flights that were shorter for the entire campaign. We increased the limits for the Aragog flights that allowed deeper discharges of the batteries to be performed as we gained more proficiency in operating the vehicles. This led to a larger error as shown by Table 11 and the corresponding Fig. 36. These indicate a much larger spread in the error in the SoE from the truth value for both the Chem and Circ models, both even having a 30 percent outlier. This could be because the models have a more difficult time capturing the battery dynamics when points well past the “knee” point (Fig. 1) are permitted in the set of comparison flights.

Table 11. Box plot distribution values, SoE difference from truth: 16 Aragog T18 flights, quiet tuning, 8-second moving average.

Box plot value	Chem	Circ
minimum	-9.5604	-2.6067
median	-0.3459	3.4523
maximum	32.1690	31.5515
lower fourth (quartile)	-5.2349	-0.1209
upper fourth (quartile)	5.1977	6.6071
IQR	10.4327	6.7280
$\mu\ (mean)$	1.9526	3.4523
$\sigma\ (std.dev.)$	10.7351	8.6679

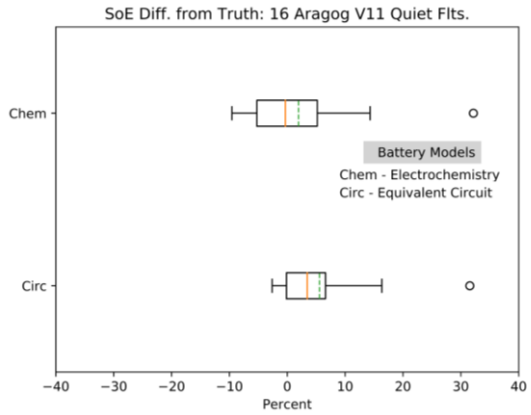

Figure 36. SoE difference from truth: 16 Aragog T18 flights, quiet tuning, 8-second moving average, mean value is dashed green line.

9.3. Performance of battery model SoE estimate at landing with one standard deviation stochastic input noise tuning, no moving average (research configuration)

We now describe our process of capturing the variation in the remaining flying time (RFT) and EoD estimate by varying the model charge states based on the input power with the addition of Gaussian noise. We varied the charge states of the Circ model and the charge and voltage states of the Chem model. We used a one standard deviation (one-sigma) tuning of the input power variation. Since the flights are dominated by the power required to hover, we could think of the flight as multiple 60 second samples from a time history with input noise added to give one sigma variation. We did not use three sigma variation because of stability problems with the electrochemistry model (Chem), and to be able to make a comparison with the equivalent circuit model (Circ). It is our belief that the larger variation would cause the Unscented Kalman Filter sigma point calculation to have negative square roots in the Cholesky factorization of the prediction error covariance matrix. We attempt to reduce this issue through constraints that biased the estimated voltage of a discharge through a bias (increase) of the internal resistance of the battery. For a Gaussian (normal) distribution, a one-sigma variation would imply a confidence of capturing 68.3 percent of the possible variation, a three-sigma variation would imply a confidence of 99.7 percent of capturing the possible variation. In our case there are tails of the distribution (Fig. 31, Fig. 32 and Fig. 33) that deviate from a normal distribution, especially if we perform deep discharges or have extremes in the wind gust variation.

Table 12 has the values of the box plots shown in Fig. 37. Likewise, Table 13 has the box plots shown in Fig. 38. We point out the interquartile range (IQR) is much smaller for the 16 Aragog Tarot 18 vehicle flights as compared with the seven DJI S1000 flights. They both were simulated with one end of discharge (EoD) projection. We explored use of a family of 60 s subset records as compared with the larger set used for our EoD plots but did not see anything occurring that deviated greatly from the larger set. One factor that may account for the difference in the skewness and width of the IQRs is that the flights in Fig. 38 were done in warmer conditions, during August and September 2022, and less gusty wind conditions than those found for the flights of Fig. 37 that were done in October and November 2019. That may account for the reduced skew to the right of the distribution for Aragog done in the summer months as compared with the Cerf flights done in autumn. Paradoxically the flights with the larger one-sigma charge state variation were more symmetrical about the median values. The Chem model also exhibited a tighter IQR spread even with the increased input variation without any 8-second moving average. If just the short, quietly-tuned Aragog flights along with the quietly-tuned Cerf flights are considered, then they have similar spread (Fig. 34 and Fig 35). The larger set of Aragog flights with quiet tuning has the largest IQR for the Chem model and the greatest difference maximum to minimum (Fig. 36).

Table 12. Box plot distribution values, SoE difference from truth: 7 Cerf DJI S1000 flights, best 1 σ tuning.

Box plot value	Chem	Circ
minimum	-17.7896	-11.9968
median	-13.5242	-6.8472
maximum	4.7319	10.6212
lower fourth (quartile)	-15.5909	-9.9201
upper fourth (quartile)	-9.3073	-2.7462
IQR	6.2836	7.1739
$\mu\ (mean)$	-10.9112	-4.7936
$\sigma\ (std.dev.)$	7.1199	7.2009

Table 13. Box plot distribution values, SoE difference from truth: 16 Aragog T18 flights, best 1 σ tuning.

Box plot value	Chem	Circ
minimum	-18.9115	-11.2336
median	-6.3235	-4.1552
maximum	2.7698	6.5404
lower fourth (quartile)	-7.6688	-6.7649
upper fourth (quartile)	-5.3964	-1.3277
IQR	2.2724	5.4371
$\mu\ (mean)$	-6.7813	-3.6323
$\sigma\ (std.dev.)$	4.7784	4.8721

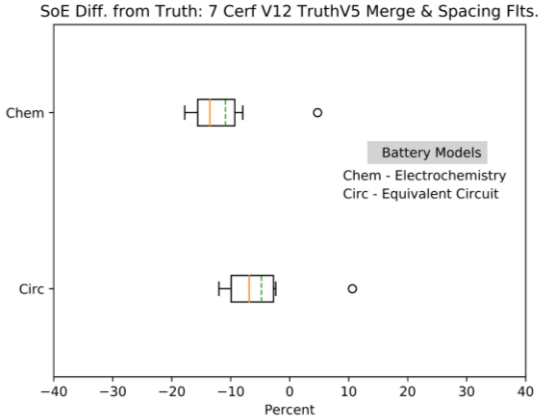

Figure 37. SoE difference from truth: 7 Cerf DJI S1000 Flights, 1 σ Tuning, mean value is dashed green line.

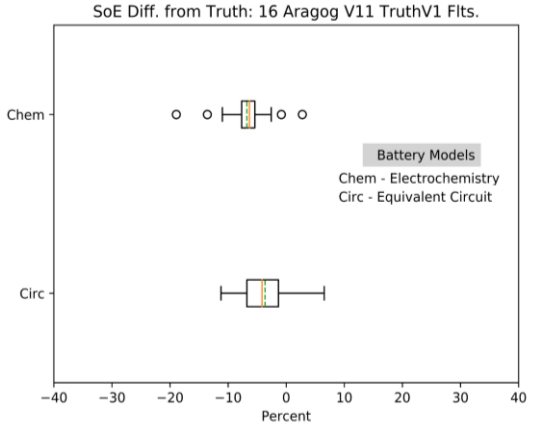

Figure 38. SoE difference from truth: 16 Aragog T18 flights, 1 σ tuning, mean value is dashed green line.

This case also has the greatest outlier seen in both the Chem and Circ models. This may be because these runs tested the lowest discharges made during the flight campaign. One flight showed less than 19 percent SoC in ground truth and required compromise tuning of the two models to keep them together for the RFT and SoC estimates. This would be a good reason to restrict flying to discharges that end before the “knee” region of Fig. 1 is entered.

10. Conclusion

The use of two octocopters and two battery capacity models allowed us to compare the behavior across flights done in warm weather conditions, cool weather conditions, and in between. We used randomized states derived from randomized current and voltage input values to perform an analysis while in a ride-along configuration with other research projects.

The distribution of the state of energy as compared with its truth value indicate a ±10

to ±15 percent accuracy. We used an 8-second moving average and a quieter tuning of the model states to make the remaining flying time estimates usable for an operator display and for other applications. This averaging seems to skew the box plot distribution of the accuracy to the right. Wind gusts also seem to skew the ground truth accuracy comparison to the right. We noticed that the accuracy seems to be degraded if a flight operates past the "knee" point of the low-current battery discharge curve, where the battery discharge becomes nonlinear. Operationally, batteries would last longer if the discharge did not go too deep. Staying away from the "knee" point would help prediction accuracy as well as longevity at the expense of flight duration.

One of the factors that we found difficult to model was the temperature variation of the voltage estimation. In considering the reliability of UAS operations and the robustness of the software, the equivalent circuit model was shown to be much more robust due to its simplicity and fewer states. The electrochemistry model encountered singular conditions of various causes. The Redlich-Kister expansion of the nonideal Gibbs free energy had the denominator of its underlying equations go to zero. The Butler-Volmer calculation also had singularities that need to be dealt with. We attempted to work-around cases that became singular, but further work is needed to fix these problems properly.

Our attempt to get the remaining flying time estimate to agree with the ground truth and to get the SoC to agree with ground truth led to tight constraints for the Chem model battery parameter identification. Our work-around overestimated the battery capacity as suggested by (Daigle 2016b) for both the Circ and Chem models. This prevented the model charge states running out of charge before the landing occurs for the flights where the SoC went below 20 percent.

The Cholesky factorization used in the Sigma point calculation of the Unscented Kalman Filter leads to the matrix square root evaluation having negative arguments. We attempted to avoid imaginary solutions so that the CFS C/C++ code did not have the complexity of complex numbers.

We tightened constraints on the internal resistance and on the battery dynamics time constants that degraded the performance of the voltage estimation. A possible improvement for future work is to consider the truth measurement of the internal resistance based on the initial application of the full hovering load. We noticed that our case with one-sigma parameter variation was not very robust (we had even wanted to use 3-sigma variation). However, the quiet tuning with the 8-second moving average work-around seemed to work robustly. The Circ equivalent circuit model with the quiet tuning may be ready to use for a reliable system, but the Chem electrochemistry model still needs work before general use.

Reference

Atkins, P., Paula, J., Keeler, J., *Atkins' Physical Chemistry Eleventh Edition*, Oxford, UK, Oxford University Press, 2018, pp. 221.

Daigle, M., Prognostics algorithm library [computer software]. https://github.com/nasa/PrognosticsAlgorithmLibrary; 2016a.

Daigle, M., Prognostics model library [computer software]. https://www.github.com/nasa/PrognosticsModelLibrary; 2016b.

Daigle, M., & Goebel, K. (2013a) "Model-based Prognostics with Concurrent Damage Progression Processes", IEEE Transactions on Systems, Man, and Cybernetics: Systems, vol. 43, no. 4, pp. 535-546, May 2013.

Daigle, M., & Kulkarni, C. (2013b). "Electrochemistry-based Battery Modeling for Prognostics," in Annual Conference of the Prognostics and Health Management Society, New Orleans, 2013.

Daigle, M., & Sankararaman, S. (2016). Predicting Remaining Driving Time and Distance of a Planetary Rover Under Uncertainty, ASCE-ASME Journal of Risk and Uncertainty in Engineering Systems Part B: Mechanical Engineering, December 2016, Vol. 2 /041001-1.

Econfly, 2014. Product Review DJI 1552 Folding Propeller https://www.dronevibes.com/forums/threads/product-review-dji-1552-folding-propeller.18704/.

Engel, S. J., Gilmartin B. J., Bongort, K., & Hess, A. (2000). Prognostics, the real issues involved with predicting life remaining. *2000 IEEE Aerospace Conference. Proceedings* (Cat. No.00TH8484). 6. 2000. p. 457–469 vol.6. http://dx.doi.org/10.1109/AERO.2000.877920.

Eure, K. & Hogge, E. (2022). "Exploration of an Adaptive Routine for Battery Modeling". NASA/TM-2022-0000668.

Faraday, M., "Experimental Researches in Electricity". January 1834 The Royal Society, vol 124, https://doi.org/10.1098/rstl.1834.0008.

Galvani, L. *De viribus electricitatis in motu musculari commentaries* (Latin), 1791, Bononiae: Ex Typographia Instituti Scientiarium, Dibner Library. Heralds of science (1980 ed.), 59.

Grewal, M. S.; & Andrews, A. P. "Applications of Kalman Filtering in Aerospace 1960 to the Present," *IEEE Control Systems Magazine*, vol. 30, no. 3, pp. 69-78, June 2010.

Hoaglin, D. C., Mosteller, F., & Tukey, J. W., *Understanding Robust and Exploratory Data Analysis*: Wiley, 1983.

Hogge, E., Bole, B., Vazquez, S., Celaya, J., Strom, T., Hill, B., Smalling, K., & Quach, C. (2015). Verification of a remaining flying time prediction system for small electric aircraft. *Annual Conference of the Prognostics and Health Management Society 2015.*

Jiang, C. S., Wang, S., Wu, B., Etse-Dabu, B., & Xiong, X. (2020) "A Novel Adaptive Extended Kalman Filtering and Electrochemical-Circuit Combined Modeling Method for the Online Ternary Battery state-of-charge Estimation," *Int. J. Electrochem. Sci.*, vol. 15, no. 10.20964, p. 9720 – 9733, 2020.

Julier, S., & Uhlmann, J., "A new extension of the Kalman filter to nonlinear systems" *AeroSense: The 11th International Symposium on Aerospace/Defense Sensing, Simulation and Controls*, 1997.

Karthikeyan, D., Sikha, G., & White, R., "Thermodynamic Model Development for Lithium Intercalation Electrodes," *Journal of Power Sources*, vol. 185, no. 2, pp. 1398-1407, 2008.

National Aeronautics and Space Administration, Goddard Space Flight Center, "Core Flight System Background and Overview," 2019, [Online] https://cfs.gsfc.nasa.gov/ and https://cfs.gsfc.nasa.gov/cFS-OviewBGSlideDeck-ExportControl-Final.pdf.

Nelder, J.A., & Mead, R. (1965) A Simplex Method for Function Minimization. *Computer Journal*, 7, 308-313. http://dx.doi.org/10.1093/comjnl/7.4.308.

Press, W., Teukolsky, S., Vetterling, W., & Flannery, B. (1996). *Numerical Recipes in C The Art of Scientific Computing Second Edition*, Cambridge, UK, Cambridge University Press, pp. 200.

Quach, C., Bole, B., Hogge, E., Vazquez, S., Daigle, M., Celaya, J., Weber, A. & Goebel, K. (2013). Battery charge depletion prediction on an electric aircraft. *Annual Conference of the Prognostics and Health Management Society 2013.*

Redlich, O., & Kister, A.T. (1948). Algebraic Representation of Thermodynamic Properties and the Classification of Solutions. *Industrial Engineering Chemistry*, 40, p. 345.

Sankararaman, S., Daigle, M., Saxena, A., & Goebel, K. (2013). Analytical Algorithms to Quantify the Uncertainty in Remaining Useful Life Prediction IEEE AC Paper #2336, Version I, Updated 0113/2013.

Sankararaman, S., & Goebel, K. (2013). Why is the Remaining Useful Life Prediction Uncertain? 2013 *Annual Conference of the Prognostics and Health Management Society 2013.*

Särkkä, S. (2013). *Bayesian Filtering and Smoothing*, New York: Cambridge University Press.

Saxena, A., Celaya, J., Balaban, E., Goebel, K., Saha, B., & Saha, S. (2008). Metrics for evaluating performance of prognostic techniques. 2008 *International Conference on Prognostics and Health Management. 2008*. p. 1–17.

Tomiska, J. (1984). Mathematical Conversions of the Thermodynamic Excess Functions Represented by the Redlich-Kister Expansion, and by the Chebyshev Polynomial Series to Power Series Representations and Vice-versa, *CALPHAD* vol. 8, no. 4, pp. 283-294.

https://dx.doi.org/10.1109/PHM.2008.4711436.

Saxena, A., Celaya, J., Saha, B., Saha, S., & Goebel, K. (2009). On applying the prognostic performance metrics. *2009 International Conference on Prognostics and Health Management*. 2009.

Saxena, A., Celaya, J., Roychoudhury, I., Saha, S., Saha, B., & Goebel, K. (2012). Designing Data-Driven Battery Prognostic Approaches for Variable Loading Profiles: Some Lessons Learned 2012 European *Conference of Prognostics and Health Management Society 2012.*

Sierra, G., Orchard, M., Goebel, K., & Kulkarni, C. (2018). Battery health management for small-size rotary-wing electric unmanned aerial vehicles: An efficient approach for constrained computing platforms. *Reliability Engineering & System Safety*. doi: https://doi.org/10.1016/j.ress.2018.04.030.

Smalling, K. S., & Jordan, T., System-Wide Safety 2021 Flight Campaign Stage 3, Final Brief to the NASA Eastern Region Airworthiness Review Board August 11, 2022. LPR 1710.18.

Stepniewski, W. Z., (1979). Rotary-wing Aerodynamics. Volume I: Basic Theories of Rotor Aerodynamics with Application to Helicopters. vol. I. Washington, United States: National Aeronautics and Space Administration NASA, Scientific and Technical Information Office; p. 44–90. Chapter: Momentum Theory.

Teubert, C., Daigle, M., Sankararaman, S., Watkins, J., & Goebel, K. (2016, December). Generic software architecture for prognostics (GSAP). Retrieved from https://github.com/nasa/GSAP.

Volta, A. (20 March 1800). Banks, J. (ed.). "On the Electricity excited by the mere Contact of conducting Substances of different kinds". Philosophical Transactions of the Royal Society (in French). 90: 403. https://doi:10.1098/rspl.1800.0018.

Young, S., Ancel, E., Moore, A., Dill, E., Quach, C., Foster, J., Darafsheh, K., Smalling, K., Vazquez, S., Evans, E., Okolo,

W., Corbetta, M., Ossenfort, J., Watkins, J., Kulkarni, C., & Spirkovska, L. (2020). “Architecture and Information Requirements to Assess and Predict Flight Safety Risks During Highly Autonomous Urban Flight Operations”, NASA-TM-2020-220440.

Appendix

A. Description of the Electrochemistry Model

The basic kinetics for the electrochemistry model are derived from the chemical reactions that take place at the electrodes and are shown in equations A.1 through A.4 of (Daigle & Kulkarni, 2013). Equations A.1 and A.2 are the reactions at the electrodes during a discharge. During discharge, an oxidation reaction takes place at the negative electrode resulting in lithium ions and electrons. The electrons travel from the surface of the negative electrode to the surface of the positive electrode leaving the surface potential of the negative

$$Li_xC \rightarrow C + xLi^+ + xe^- \quad \text{A.1}$$

$$Li_{1-x}CoO_2 + xLi^+ + xe^- \rightarrow LiCoO_2 \quad \text{A.2}$$

electrode increased and the surface potential of the positive electrode decreased causing them to converge towards the same potential. This means that the voltage will decrease as the voltage across the battery is the difference between the negative electrode surface potential and the positive electrode surface potential. The lithium ions travel from the bulk of the negative electrode to the bulk of the positive electrode through the electrolyte. A reduction reaction occurs at the positive electrode when lithium ions diffuse into the surface and the electrons diffuse into the bulk. The result is the increase in the surface potential at the positive electrode which counters the decrease from the initial introduction of the electrons.

Equations A.3 and A.4 are the reactions that take place at the electrodes during charging. During charging, oxidation occurs at the positive electrode and results in lithium ions and electrons as products. The electrons travel from the surface

$$C + xLi^+ + xe^- \rightarrow Li_xC \quad \text{A.3}$$

$$LiCoO_2 \rightarrow Li_{1-x}CoO_2 + xLi^+ + xe^- \quad \text{A.4}$$

of the positive electrode to the surface of the negative electrode resulting in an increase in the surface potential at the positive electrode and a decrease in the surface potential at the negative electrode. The surface potentials diverge during charging which increases the voltage. The lithium ions travel from the bulk of the positive electrode to the bulk of the negative electrode through the electrolyte. A reduction reaction takes place at the negative electrode when lithium ions diffuse into the surface and electrons diffuse into the bulk. This results in an increase in the surface potential at the negative electrode which counters the decrease in potential from the introduction of the electrons that traversed from the positive electrode surface.

To define the electrochemistry-based model, the relevant voltages and how they impact the voltage of the battery must be detailed. First, the battery voltage that the model is capturing, and our system is measuring, is seen in Fig. 39 (Daigle et al. 2013b) to be the difference in potential between the surfaces of the negative and positive electrodes.

The voltages that factor into the determination of the battery voltage can be stated in relation to how they detract from the ideal voltage. This voltage is defined as the difference between $V_{U,p}$ and $V_{U,n}$. The first set of voltages that detract from the equilibrium voltage are known as ohmic voltage drops. The ohmic voltages are comprised of the electrolyte ohmic voltage denoted V_e, the solid phase ohmic voltage of the positive electrode denoted $V_{s,p}$, and the solid phase ohmic voltage of the negative electrode denoted $V_{s,n}$. The second set of voltages that detract from the equilibrium voltage are known as surface overpotentials

and are a result of charge transfer resistance and solid electrolyte interface kinetics (Daigle et al. 2013b). The surface overpotentials are comprised of a negative electrode surface overpotential denoted $V_{\eta,p}$ and a positive electrode surface overpotential denoted $V_{\eta,n}$.

The state definition, the input, the output, and the relevant model variables are defined in equations A.5 through A.7.

$$x(t) = [\, q_{s,p}\ q_{b,p}\ q_{b,n}\ q_{s,n}\ V_o'\ V_{\eta,p}'\ V_{\eta,n}' \,] \quad \text{A.5}$$

$$u(t) = [\, i_{app} \,] \quad \text{A.6}$$

$$y(t) = [\, V \,] \quad \text{A.7}$$

The state vector is defined in equation A.5 and consists of the positive electrode surface charge $q_{s,p}$, the positive electrode bulk charge $q_{b,p}$, the negative electrode bulk charge $q_{b,n}$, the negative electrode surface charge $q_{s,n}$, the sum of the ohmic voltage contributions V_o', the positive electrode overpotential $V_{\eta,p}'$, and the negative electrode overpotential $V_{\eta,n}'$. The input vector is defined in equation C.6 and consists of the discharge current i_{app}. The output vector is defined in equation A.7 and consists of the battery model voltage V,V_m.

The state transition equations for the electrode charges incorporate the discharge current and diffusion, as shown in equations A.8 through A.12 (Daigle et al. 2013b). Inter-electrode electron flow occurs primarily at the surface of the electrodes. Hence, the current does not have a direct impact on charge at the bulk of the electrodes. Indirectly, the current changes the concentration gradient of lithium ions between the surface and the bulk of the electrodes which impacts diffusion and in turn the charge at the bulk of the electrodes. The cumulative charge equations are shown in equations A.13 through A.15 (Daigle et al. 2013b).

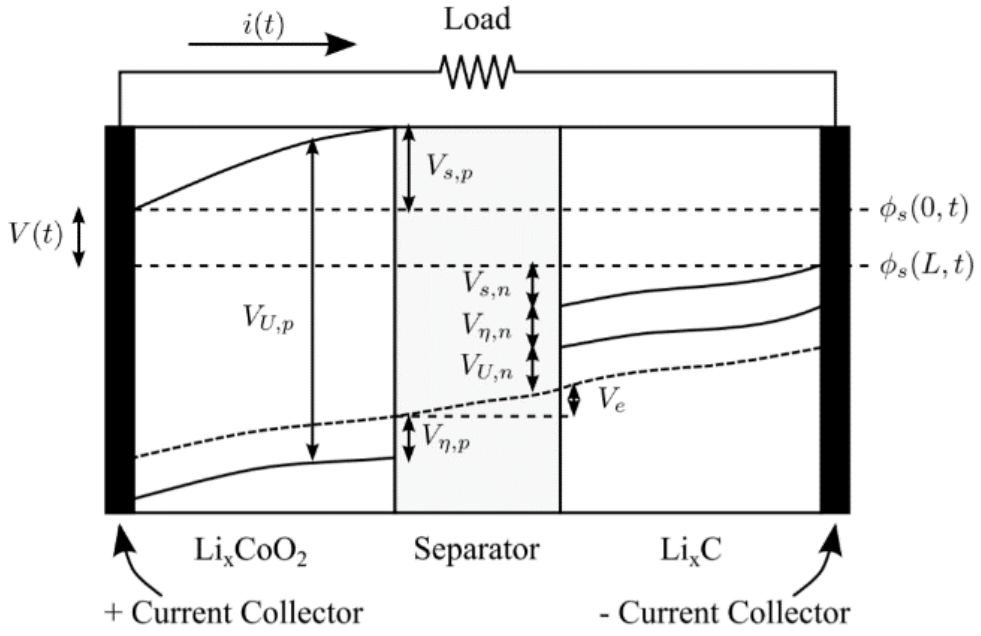

Figure 39. Battery Diagram (Daigle et al. 2013).

$$\dot{q}_{s,p} = i_{app} + \dot{q}_{bs,p} \quad \text{A.8}$$

$$\dot{q}_{b,p} = -\dot{q}_{bs,p} \quad \text{A.9}$$

$$\dot{q}_{b,n} = -\dot{q}_{bs,n} \quad \text{A.10}$$

$$\dot{q}_{s,n} = -i_{app} + \dot{q}_{bs,n} \quad \text{A.11}$$

$$\dot{q}_{bs,i} = \frac{1}{t_{diffusion}}\left(c_{b,i} - c_{s,i}\right) \quad \text{A.12}$$

$$i = p, n$$

$$q_p = q_{s,p} + q_{b,p} \quad \text{A.13}$$

$$q_n = q_{s,n} + q_{b,n} \quad \text{A.14}$$

$$q_{max} = q_p + q_n \quad \text{A.15}$$

These charge equations are coupled directly with the concentration and lithium mole fraction equations shown in equations A.16 through A.20 (Daigle et al. 2013b).

$$c_{b.i} = \frac{q_{b.i}}{v_{b.i}} \quad \text{A.16}$$

$$c_{s,i} = \frac{q_{s,i}}{v_{s,i}} \quad \text{A.17}$$

$$x_i = \frac{q_i}{q_{max}} \quad \text{A.18}$$

$$x_{s,i} = \frac{q_{s,i}}{q_{s,i,max}} \quad \text{A.19}$$

$$x_{b,i} = \frac{q_{b,i}}{q_{b,i,max}} \quad \text{A.20}$$

Here v refers to volume and the subscript i refers to the positive or negative electrode. For Li_xCoO_2, the lithium-ion mole fraction for the positive electrode x_p must be at least 0.4, Li cannot be reversibly removed beyond that (Karthikeyan et al. 2008). Since $x_p + x_n = 1.0$, the lithium-ion mole fraction at the negative electrode must be no greater than 0.6.

The equations to solve for the cumulative ohmic voltage, the surface overpotentials, and the intermediate variables are shown in equations A.21 through A.29. In equation A.21, U_0 is the reference potential. In equations A.21 through A.29, R is the universal gas constant, T is the electrode temperature, n is the number of electrons transferred in from the chemical reaction in equation A.1, and F is Faraday's constant.

$$V_{u,i} = U_{0,i} + \frac{RT}{nF}\ln\left(\frac{1 - x_{s,i}}{x_{s,i}}\right) + V_{INT,i} \quad \text{A.21}$$

$$V_{INT,i} = \frac{1}{nF}\sum_{k=0}^{N_i} A_{i,k}((2x_{s,i} - 1)^{k+1} - \frac{2x_{s,i}k\left(1 - x_{s,i}\right)}{(2x_{s,i} - 1)^{1-k}}) \quad \text{A.22}$$

$$V_o = i_{app}R_o \quad \text{A.23}$$

$$V_{\eta,i} = \frac{RT}{F\alpha}\text{arcsinh}\,(\frac{J_i}{2J_{i0}}) \quad \text{A.24}$$

$$J_i = \frac{i_{app}}{S_i} \quad \text{A.25}$$

$$J_{i0} = k_i(1 - x_{s,i})^{\alpha}(x_{s,i})^{1-\alpha} \quad \text{A.26}$$

$$\dot{V}_o' = \frac{V_o - V_o'}{\tau_o} \quad \text{A.27}$$

$$\dot{V}_{\eta,p}' = \frac{V_{\eta,p} - V_{\eta,p}'}{\tau_{\eta,p}} \quad \text{A.28}$$

$$\dot{V}_{\eta,n}' = \frac{V_{\eta,n} - V_{\eta,n}'}{\tau_{\eta,n}} \quad \text{A.29}$$

R_o is the cumulative resistance from the ohmic voltages drop, α is the symmetry factor, and S_i is the area of the electrode. The terms $\tau_{\eta,p}$, and $\tau_{\eta,n}$ denote time constants. Lastly, $A_{i,k}$ are parameters for the Redlich-Kister expansion. The Redlich-Kister expansion is used to capture the activity coefficient terms related to excess Gibbs free energy (Karthikeyan et al. 2008). For a more detailed description of the intermediate variables see (Daigle et al. 2013b).

The equation for the battery model voltage V,V_m is shown in equation A.30 and the state of charge (SoC) equations are shown in equations A.31 and A.32 Daigle et al. (2013b). The nominal SoC refers to the percent of charge left at the negative electrode while the apparent SoC refers to

the percent of charge left at the surface of the negative electrode. If the charge at the surface of the negative electrode becomes entirely depleted, discharge cannot continue until charge diffuses from the bulk of the negative electrode so long as the nominal SoC has not been entirely depleted in that instance.

$$V = V_{u,p} - V_{u,n} - V_o' - V_{\eta,p}' - V_{\eta,n}' \quad \text{A.30}$$

$$SOC_{nominal} = \frac{q_n}{0.6q_{max}} \quad \text{A.31}$$

$$SOC_{apparent} = \frac{q_{s,n}}{0.6q_{s,n,max}} \quad \text{A.32}$$

B. BHM_Circ and BHM_Chem Class Diagram

Applications BHM_Circ and BHM_Chem were derived from the GitHub open-source MATLAB code Prognostics Model Library by (Daigle, 2016b) and the Prognostics Algorithm Library by (Daigle, 2016a). We used the open-source Generic System for Prognostics (GSAP) library by (Teubert et al. 2016). Figure 40 and Fig. 41 depict a class diagram of the modules

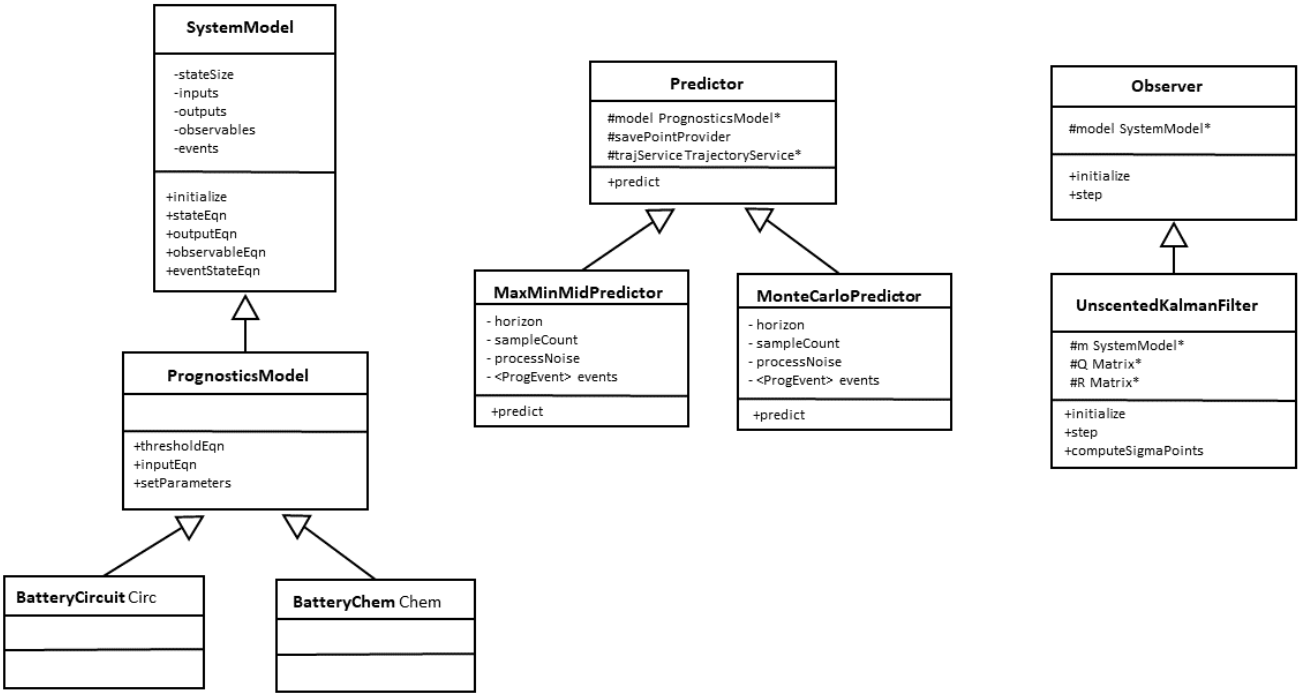

Figure 40. GSAP CFS Subset Class Diagram Part 1.

derived from the GSAP library for applications BHM_Circ and BHM_Chem.

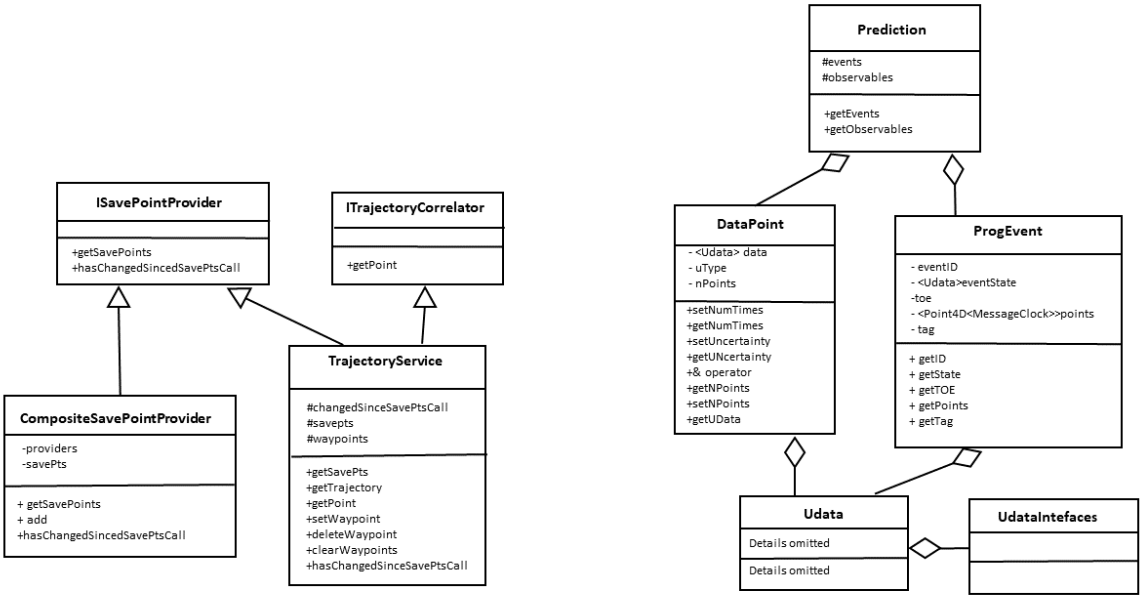

Figure 41. GSAP CFS Subset Class Diagram Part 2.